CrossMark

ORIGINAL ARTICLE

Characterising the physical and chemical properties of a young Class 0 protostellar core embedded in the Orion B9 filament

O. Miettinen[1,2] (ORCID)

Abstract Deeply embedded low-mass protostars can be used as testbeds to study the early formation stages of solar-type stars, and the prevailing chemistry before the formation of a planetary system. The present study aims to characterise further the physical and chemical properties of the protostellar core Orion B9–SMM3. The Atacama Pathfinder EXperiment (APEX) telescope was used to perform a follow-up molecular line survey of SMM3. The observations were done using the single pointing (frequency range 218.2–222.2 GHz) and on-the-fly mapping methods (215.1–219.1 GHz). These new data were used in conjunction with our previous data taken by the APEX and Effelsberg 100 m telescopes. The following species were identified from the frequency range 218.2–222.2 GHz: ^{13}CO, C^{18}O, SO, *para*-H$_2$CO, and E$_1$-type CH$_3$OH. The mapping observations revealed that SMM3 is associated with a dense gas core as traced by DCO$^+$ and *p*-H$_2$CO. Altogether three different *p*-H$_2$CO transitions were detected with clearly broadened linewidths ($\Delta v \sim 8.2$–11 km s^{-1} in FWHM). The derived *p*-H$_2$CO rotational temperature, 64 ± 15 K, indicates the presence of warm gas. We also detected a narrow *p*-H$_2$CO line ($\Delta v = 0.42$ km s^{-1}) at the systemic velocity. The *p*-H$_2$CO abundance for the broad component appears to be enhanced by two orders of magnitude with respect to the narrow line value ($\sim 3 \times 10^{-9}$ versus $\sim 2 \times 10^{-11}$). The detected methanol line shows a linewidth similar to those of the broad *p*-H$_2$CO lines, which indicates their coexistence. The CO isotopologue data suggest that the CO depletion factor decreases from $\sim 27 \pm 2$ towards the core centre to a value of $\sim 8 \pm 1$ towards the core edge. In the latter position, the N$_2$D$^+$/N$_2$H$^+$ ratio is revised down to 0.14 ± 0.06. The origin of the subfragments inside the SMM3 core we found previously can be understood in terms of the Jeans instability if non-thermal motions are taken into account. The estimated fragmentation timescale, and the derived chemical abundances suggest that SMM3 is a few times 10^5 yr old, in good agreement with its Class 0 classification inferred from the spectral energy distribution analysis. The broad *p*-H$_2$CO and CH$_3$OH lines, and the associated warm gas provide the first clear evidence of a molecular outflow driven by SMM3.

1 Introduction

Low-mass stars have main-sequence masses of $M_\star \simeq 0.08$–2 M$_\odot$, and are classified with spectral types of M7–A5 (e.g. Stahler and Palla 2005). The formation process of these types of stars begins when the parent molecular cloud core undergoes gravitational collapse (e.g. Shu et al. 1987; McKee and Ostriker 2007). In the course of time, the collapsing core centre heats up due to compression, and ultimately becomes a protostar. The youngest low-mass protostars, characterised by accretion from the much more massive envelope ($M_{\rm env} \gg M_\star$), are known as the Class 0 objects (André et al. 1993, 2000).

A curious example of a Class 0 protostellar object is SMM3 in the Orion B9 star-forming filament. This object was first uncovered by Miettinen et al. (2009; hereafter Paper I), when they mapped Orion B9 using the Large

✉ O. Miettinen
oskari@phy.hr

1 Department of Physics, University of Zagreb, Bijenička cesta 32, HR-10000 Zagreb, Croatia

2 Department of Physics, University of Helsinki, P.O. Box 64, FI-00014 Helsinki, Finland

APEX BOlometer CAmera (LABOCA) at 870 μm. In Paper I, we constructed and analysed a simple mid-infrared–submillimetre spectral energy distribution (SED) of SMM3, and classified it as a Class 0 object. The physical and chemical properties of SMM3 (e.g. the gas temperature and the level of N_2H^+ deuteration) were further characterised by Miettinen et al. (2010, 2012; hereafter referred to as Papers II and III, respectively) through molecular line observations. In Paper III, we also presented the results of our Submillimetre APEX BOlometer CAmera (SABOCA) 350 μm imaging of Orion B9. With the flux density of $S_{350\,\mu m} \simeq 5.4$ Jy, SMM3 turned out to be the strongest 350 μm emitter in the region. Perhaps more interestingly, the 350 μm image revealed that SMM3 hosts two subfragments (dubbed SMM3b and 3c) on the eastern side of the protostar, where an extension could already be seen in the LABOCA map at 870 μm. The projected distances of the subfragments from the protostar's position, 0.07–0.10 pc,[1] were found to be comparable to the local thermal Jeans length. This led us to suggest that the parent core might have fragmented into smaller units via Jeans gravitational instability.

The Orion B or L1630 molecular cloud, including Orion B9, was mapped with *Herschel* as part of the *Herschel* Gould Belt Survey (HGBS; André et al. 2010).[2] The *Herschel* images revealed that Orion B9 is actually a filamentary-shaped cloud in which SMM3 is embedded (see Fig. 2 in Miettinen and Offner 2013b). Miettinen (2012b) found that there is a sharp velocity gradient in the parent filament (across its short axis), and suggested that it might represent a shock front resulting from the feedback from the nearby expanding HII region/OB cluster NGC 2024 (∼3.7 pc to the southwest of Orion B9). Because SMM3 appears to lie on the border of the velocity gradient, it might have a physical connection to it, and it is possible that the formation of SMM3 (and the other dense cores in Orion B9) was triggered by external, positive feedback (Miettinen 2012b). Actually, the OB associations to the west of the whole Orion B cloud have likely affected much of the cloud area through their strong feedback in the form of ionising radiation and stellar winds (e.g. Cowie et al. 1979). The column density probability distribution function of Orion B, studied by Schneider et al. (2013), was indeed found to be broadened as a result of external compression.

The Class 0 object SMM3 was included in the Orion protostellar core survey by Stutz et al. (2013, hereafter S13; their source 090003). Using data from *Spitzer*, *Herschel*, SABOCA, and LABOCA, S13 constructed an improved SED of SMM3 compared to what was presented in Paper I. The bolometric temperature and luminosity—as based on the Myers and Ladd (1993) method—were found to be $T_{bol} = 36.0 \pm 0.8$ K and $L_{bol} = 2.71 \pm 0.24$ L$_\odot$. They also performed a modified blackbody (MBB) fit to the SED ($\lambda \geq 70$ μm) of SMM3, and obtained a dust temperature of $T_{dust} = 21.4 \pm 0.4$ K, luminosity of $L = 2.06 \pm 0.15$ L$_\odot$, and envelope mass of $M_{env} = 0.33 \pm 0.06$ M$_\odot$ (see their Fig. 9). The derived SED properties led S13 to the conclusion that SMM3 is likely a Class 0 object, which supports our earlier suggestion (Papers I and III).

Tobin et al. (2015) included SMM3 in their Combined Array for Research for Millimetre Astronomy (CARMA) 2.9 mm continuum imaging survey of Class 0 objects in Orion. This was the first high angular resolution study of SMM3. With a 2.9 mm flux density of $S_{2.9\,mm} = 115.4 \pm 3.9$ mJy (at an angular resolution of $2.''74 \times 2.''56$), SMM3 was found to be the second brightest source among the 14 target sources. The total (gas+dust) mass derived for SMM3 by Tobin et al. (2015), $M = 7.0 \pm 0.7$ M$_\odot$, is much higher than that derived earlier by S13 using a MBB fitting technique, which underpredicted the 870 μm flux density of the source (see Tobin et al. 2015 and Sect. 4.1 herein for further discussion and different assumptions used). Tobin et al. (2015) did not detect 2.9 mm emission from the subfragments SMM3b or 3c, which led the authors to conclude that they are starless.

Kang et al. (2015) carried out a survey of H_2CO and HDCO emission towards Class 0 objects in Orion, and SMM3 was part of their source sample (source HOPS403 therein). The authors derived a $HDCO/H_2CO$ ratio of 0.31 ± 0.06 for SMM3, which improves our knowledge of the chemical characteristics of this source, and strongly points towards its early evolutionary stage from a chemical point of view.

Finally, we note that SMM3 was part of the recent large Orion protostellar core survey by Furlan et al. (2016; source HOPS400 therein), where the authors presented the sources' panchromatic (1.2–870 μm) SEDs and radiative transfer model fits. They derived a bolometric luminosity of $L_{bol} = 2.94$ L$_\odot$ (a trapezoidal summation over all the available flux density data points), total (stellar+accretion) luminosity of $L_{tot} = 5.2$ L$_\odot$, bolometric temperature of $T_{bol} = 35$ K (following Myers and Ladd 1993 as in S13), and an envelope mass of $M_{env} = 0.30$ M$_\odot$, which are in fairly good agreement with the earlier S13 results. We note that the total luminosity derived by Furlan et al. (2016) from their best-fit model is corrected for inclination effects, and hence is higher than L_{bol}. Moreover, the aforementioned value of

---

[1]In the present work, we have adopted a distance of $d = 420$ pc to the source to be consistent with the most recent studies of SMM3 (Stutz et al. 2013; Tobin et al. 2015; Furlan et al. 2016). We note that in Papers I–III, we assumed a distance of 450 pc, which is a factor of 1.07 larger than used here.

[2]The HGBS is a *Herschel* key programme jointly carried out by SPIRE Specialist Astronomy Group 3 (SAG 3), scientists of several institutes in the PACS Consortium (CEA Saclay, INAF-IFSI Rome and INAF-Arcetri, KU Leuven, MPIA Heidelberg), and scientists of the *Herschel* Science Center (HSC). For more details, see http://gouldbelt-herschel.cea.fr.

M_{env} refers to a radius of 2 500 AU (=0.012 pc), which corresponds to an angular radius of about $6''$ at the distance of SMM3, while a similar envelope mass value derived by S13 refers to a larger angular scale as a result of coarser resolution of the observational data used (e.g. $19''$ resolution in their LABOCA data).

In the present study, we attempt to further add to our understanding of the physical and chemical properties of SMM3 by means of our new molecular line observations. We also re-analyse our previous spectral line data of SMM3 in a uniform manner to make them better comparable with each other. This paper is outlined as follows. The observations and the observational data are described in Sect. 2. The immediate observational results are presented in Sect. 3. The analysis of the observations is described in Sect. 4. The results are discussed in Sect. 5, and the concluding remarks are given in Sect. 6.

2 Observations, data, and data reduction

2.1 New spectral line observations with APEX

2.1.1 Single-pointing observations

A single-pointing position at $\alpha_{2000.0} = 05^h42^m45\overset{s}{.}24$, and $\delta_{2000.0} = -01°16'14''\!.0$ (i.e. the *Spitzer* 24 μm peak of SMM3) was observed with the 12-metre APEX telescope[3] (Güsten et al. 2006) in the frequency range $\sim$218.2–222.2 GHz. The observations were carried out on 20 August 2013, when the amount of precipitable water vapour (PWV) was measured to be 1.3 mm, which corresponds to a zenith atmospheric transmission of about 93%.

As a front end we used the APEX-1 receiver of the Swedish Heterodyne Facility Instrument (SHeFI; Belitsky et al. 2007; Vassilev et al. 2008a,b). The APEX-1 receiver operates in a single-sideband (SSB) mode using sideband separation mixers, and it has a sideband rejection ratio better than 10 dB. The backend was the RPG eXtended bandwidth Fast Fourier Transform Spectrometer (XFFTS; see Klein et al. 2012) with an instantaneous bandwidth of 2.5 GHz and 32 768 spectral channels. The spectrometer consists of two units, which have a fixed overlap region of 1.0 GHz. The resulting channel spacing, 76.3 kHz, corresponds to 104 m s^{-1} at the central observed frequency of 220 196.65 MHz. The beam size (Half-Power Beam Width or HPBW) at the observed frequency range is $\sim 28''\!.1$–$28''\!.6$.

The observations were performed in the wobbler-switching mode with a $100''$ azimuthal throw between two positions on sky (symmetric offsets), and a chopping rate of $R = 0.5$ Hz. The total on-source integration time was

34 min. The telescope focus and pointing were optimised and checked at regular intervals on the planet Jupiter and the variable star R Leporis (Hind's Crimson Star). The pointing was found to be accurate to $\sim 3''$. The typical SSB system temperatures during the observations were in the range $T_{sys} \sim$ 130–140 K. Calibration was made by means of the chopper-wheel technique, and the output intensity scale given by the system is the antenna temperature corrected for the atmospheric attenuation ($T_A^\star$). The observed intensities were converted to the main-beam brightness temperature scale by $T_{MB} = T_A^\star/\eta_{MB}$, where $\eta_{MB} = 0.75$ is the main-beam efficiency at the observed frequency range. The absolute calibration uncertainty is estimated to be about 10%.

The spectra were reduced using the Continuum and Line Analysis Single-dish Software 90 (CLASS90) program of the GILDAS software package.[4] The individual spectra were averaged, and the resulting spectra were Hanning-smoothed to a velocity resolution of 208 m s^{-1} to improve the signal-to-noise (S/N) ratio. Linear (first-order) baselines were determined from the velocity ranges free of spectral line features, and then subtracted from the spectra. The resulting 1σ rms noise levels at the smoothed velocity resolution were $\sim$6.3–19 mK on a $T_A^\star$ scale, or $\sim$8.4–25.3 mK on a T_{MB} scale.

The line identification from the observed frequency range was done by using Weeds, which is an extension of CLASS (Maret et al. 2011), and the JPL[5] and CDMS[6] spectroscopic databases. The following spectral line transitions were detected: ^{13}CO(2–1), C^{18}O(2–1), SO(5_6–4_5), *para*-H$_2$CO($3_{0,3}$–$2_{0,2}$), *para*-H$_2$CO($3_{2,2}$–$2_{2,1}$), *para*-H$_2$CO($3_{2,1}$–$2_{2,0}$), and E$_1$-type CH$_3$OH(4_2–3_1). Selected spectroscopic parameters of the detected species and transitions are given in Table 1. We note that the original purpose of these observations was to search for glycolaldehyde (HCOCH$_2$OH) line emission near 220.2 GHz (see Jørgensen et al. 2012; Coutens et al. 2015). However, no positive detection of HCOCH$_2$OH lines was made.

2.1.2 Mapping observations

The APEX telescope was also used to map SMM3 and its surroundings in the frequency range $\sim$215.1–219.1 GHz. The observations were done on 15 November 2013, with the total telescope time of 2.9 hr. The target field, mapped

---

Table 1 The observed molecular spectral lines and selected spectroscopic parameters

Transition	ν [MHz]	E_u/k_B [K]	μ [D]	n_{crit} [cm^{-3}]	Rotational constants and Ray's parameter (κ)
p-NH$_3$(J, $K = 1$, 1)	23 694.4955	23.26	1.4719 (= μ_C)	3.9×10^{3}[a]	$A = B = 298\,192.92$ MHz, $C = 186\,695.86$ MHz; $\kappa = +1 \Rightarrow$ oblate symmetric top
p-NH$_3$(J, $K = 2$, 2)	23 722.6333	64.45	1.4719 (= μ_C)	3.08×10^{3}[a]	...
DCO$^+$($J = 3$–2)	216 112.5766[b]	20.74	3.888 (= μ_A)	2.0×10^{6}[c]	$B = 36\,019.76$ MHz; linear molecule
p-H$_2$CO($J_{K_a, K_c} = 3_{0,3}$–$2_{0,2}$)	218 222.192	20.96	2.331 (= μ_A)	2.8×10^{6}[c]	$A = 281\,970.5$ MHz, $B = 38\,833.98$ MHz, $C = 34\,004.24$ MHz; $\kappa = -0.961 \Rightarrow$ prolate asymmetric top
CH$_3$OH-E$_1$($J_{K_a, K_c} = 4_{2,2}$–$3_{1,2}$)	218 440.050	45.46	0.899 (= μ_A) -1.44 (= μ_B)	4.7×10^{6}[c]	$A = 127\,523.4$ MHz, $B = 24\,690.2$ MHz, $C = 23\,759.7$ MHz; $\kappa = -0.982 \Rightarrow$ prolate asymmetric top
p-H$_2$CO($J_{K_a, K_c} = 3_{2,2}$–$2_{2,1}$)	218 475.632	68.09	2.331 (= μ_A)	1.2×10^{6}[c]	...
p-H$_2$CO($J_{K_a, K_c} = 3_{2,1}$–$2_{2,0}$)	218 760.066	68.11	2.331 (= μ_A)	2.6×10^{6}[c]	...
C^{18}O($J = 2$–1)	219 560.3568	15.81	0.11079 (= μ_A)	2.0×10^{4}[c]	$B = 54\,891.42$ MHz; linear molecule
SO($N_J = 5_6$–4_5)	219 949.442	34.98	1.55 (= μ_A)	2.4×10^{6}[d]	$B = 21\,523.02$ MHz; linear molecule
^{13}CO($J = 2$–1)	220 398.7006[e]	15.87	0.11046 (= μ_A)	2.0×10^{4}[c]	$B = 55\,101.01$ MHz; linear molecule
C^{17}O($J = 2$–1)	224 714.199[f]	16.18	0.11034 (= μ_A)	2.1×10^{4}[c]	$B = 56\,179.99$ MHz; linear molecule
N$_2$D$^+$($J = 3$–2)	231 321.912[g]	22.20	3.40 (= μ_A)	1.9×10^{6}[h]	$B = 38\,554.71$ MHz; linear molecule
N$_2$H$^+$($J = 3$–2)	279 511.832[g]	26.83	3.40 (= μ_A)	3.3×10^{6}[h]	$B = 46\,586.86$ MHz; linear molecule
DCO$^+$($J = 4$–3)	288 143.855[i]	34.57	3.888 (= μ_A)	1.9×10^{7}[c]	$B = 36\,019.76$ MHz; linear molecule

Note: The spectroscopic data were compiled from the JPL database except in the cases of CH$_3$OH and ^{13}CO where the data were taken from the CDMS. In columns (2)–(5) we list the rest frequency, upper-state energy divided by the Boltzmann constant, permanent electric dipole moment, and critical density at 10 K unless otherwise stated. In the last column, we give the rotational constants (A, B, C) and the Ray's asymmetry parameter, which is defined by $\kappa = (2B - A - C)/(A - C)$

[a] From Maret et al. 2009

[b] Frequency of the strongest hyperfine component $F = 4$–3 (JPL)

[c] To calculate n_{crit}, we used the Einstein A coefficients and collision rates (C_{ul}) adopted from the Leiden Atomic and Molecular Database (LAMDA; Schöier et al. 2005); http://home.strw.leidenuniv.nl/~moldata/

[d] A value of C_{ul} at 60 K from LAMDA was used (i.e. at the lowest temperature value reported in the database)

[e] Frequency of the strongest hyperfine component $F = 5/2$–3/2 (CDMS)

[f] Frequency of the strongest hyperfine component $F = 9/2$–7/2 (Ladd et al. 1998)

[g] Frequency of the strongest hyperfine component F_1, $F = 4$, 5–3, 4 (Pagani et al. 2009; their Tables 4 and 10)

[h] To calculate n_{crit}, we used the Einstein A coefficients from Pagani et al. (2009), and the N$_2$H$^+$–H$_2$ collision rate from LAMDA

[i] Frequency of the strongest hyperfine component $F = 5$–4 (JPL)

using the total power on-the-fly mode, was $5' \times 3'.25$ (0.61×0.40 pc^2) in size, and centred on the coordinates $\alpha_{2000.0} = 05^h42^m47^s.071$, and $\delta_{2000.0} = -01°16'33''.70$. At the observed frequency range, the telescope HPBW is $\sim28''.5$–29''. The target area was scanned alternately in right ascension and declination, i.e. in zigzags to ensure minimal striping artefacts in the final data cubes. Both the angular separation between two successive dumps and the step size between the subscans was 9''.5, i.e. about one-third the HPBW. We note that to avoid beam smearing, the readout spacing should not exceed the value HPBW/3. The

dump time was set to one second. The front end/backend system was composed of the APEX-1 receiver, and the 2.5 GHz XFFTS with 32 768 channels. The channel spacing, 76.3 kHz, corresponds to 105 m s^{-1} at the central observed frequency of 217 104.98 MHz.

The focus and pointing measurements were carried out by making CO(2–1) cross maps of the planet Jupiter and the M-type red supergiant α Orionis (Betelgeuse). The pointing was found to be consistent within $\sim3''$. The amount of PWV was ~0.6 mm, which translates into a zenith transmission of about 96%. The data were calibrated using the

standard chopper-wheel method, and the typical SSB system temperatures during the observations were in the range $T_{sys} \sim 120$–130 K on a $T_A^{\star}$ scale. The main-beam efficiency needed in the conversion to the main-beam brightness temperature scale is $\eta_{MB} = 0.75$. The absolute calibration uncertainty is about 10%.

The CLASS90 program was used to reduce the spectra. The individual spectra were Hanning-smoothed to a velocity resolution of 210 m s^{-1} to improve the S/N ratio of the data, and a third-order polynomial was applied to correct the baseline in the spectra. The resulting 1σ rms noise level of the average smoothed spectra were about 90 mK on a $T_A^{\star}$ scale. The visible spectral lines, identified by using Weeds, were assigned to DCO$^+$(3–2) and p-H$_2$CO($3_{0,3}$–$2_{0,2}$) (see Table 1 for details). The latter line showed an additional velocity component at $v_{LSR} \simeq 1.5$ km s^{-1}, while the systemic velocity of SMM3 is about 8.5 km s^{-1}. The main purpose of these mapping observations was to search for SiO(5–4) emission at 217 104.98 MHz, but no signatures of this shock tracer were detected.

The spectral-line maps were produced using the Grenoble Graphic (GreG) program of the GILDAS software package. The data were convolved with a Gaussian of 1/3 times the HPBW, and hence the effective angular resolutions of the final DCO$^+$(3–2) and p-H$_2$CO($3_{0,3}$–$2_{0,2}$) data cubes are 30$''$7 and 30$''$4, respectively. The average 1σ rms noise level of the completed maps was $\sigma(T_{MB}) \sim 100$ mK per 0.21 km s^{-1} channel.

2.2 Previous spectral line observations

In the present work, we also employ the *para*-NH$_3$(1, 1) and (2, 2) inversion line data obtained with the Effelsberg 100 m telescope[7] as described in Paper II. The angular resolution (full-width at half maximum or FWHM) of these observations was 40$''$. The original channel separation was 77 m s^{-1}, but the spectra were smoothed to the velocity resolution of 154 m s^{-1}. We note that the observed target position towards SMM3 was $\alpha_{2000.0} = 05^h42^m44\overset{s}{.}4$, and $\delta_{2000.0} = -01°16'03\overset{''}{.}0$, i.e. $\sim16\overset{''}{.}7$ northwest of the new target position (Sect. 2.1.1).

In Paper III, we presented the C^{17}O(2–1), DCO$^+$(4–3), N$_2$H$^+$(3–2), and N$_2$D$^+$(3–2) observations carried out with APEX towards the aforementioned NH$_3$ target position. Here, we will employ these data as well. The HPBW of APEX at the frequencies of the above transitions is in the range 21$''$7–27$''$8, and the smoothed velocity resolution is 260 m s^{-1} for N$_2$H$^+$ and DCO$^+$, and 320 m s^{-1} for C^{17}O and N$_2$D$^+$. For further details, we refer to Paper III. Spectroscopic parameters of the species and transitions described in this subsection are also tabulated in Table 1.

2.3 Submillimetre dust continuum data

In the present study, we use our LABOCA 870 µm data first published in Paper I. However, we have re-reduced the data using the Comprehensive Reduction Utility for SHARC-2 (Submillimetre High Angular Resolution Camera II) or CRUSH-2 (version 2.12-2) software package[8] (Kovács 2008), as explained in more detail in the paper by Miettinen and Offner (2013a). The resulting angular resolution was 19$''$86 (FWHM), and the 1σ rms noise level in the final map was 30 mJy beam^{-1}. Measuring the flux density of SMM3 inside an aperture of radius equal to the effective beam FWHM, we obtained a value of $S_{870\,\mu m} = 1.58 \pm 0.29$ Jy, where the uncertainty includes both the calibration uncertainty ($\sim10\%$) and the map rms noise around the source (added in quadrature).

The SABOCA 350 µm data published in Paper III are also used in this study. Those data were also reduced with CRUSH-2 (version 2.03-2). The obtained angular resolution was 10$''$6 (FWHM), and the 1σ rms noise was ~60 mJy beam^{-1}. Again, if the flux density is calculated using an aperture of radius 10$''$6, we obtain $S_{350\,\mu m} = 4.23 \pm 1.30$ Jy, where the quoted error includes both the calibration uncertainty ($\sim30\%$) and the local rms noise. This value is about 1.3 times lower than the one reported in Paper III (5.4 ± 1.6 Jy, which was based on a clumpfind analysis above a 3σ emission threshold). The APEX dust continuum flux densities of SMM3 are tabulated in Table 2.

2.4 Far-infrared and millimetre data from the literature

For the purpose of the present study, we use the far-infrared (FIR) flux densities from S13, and the 2.9 mm flux density of $S_{2.9\,mm} = 115.4 \pm 3.9$ mJy from Tobin et al. (2015). Stutz et al. (2013) employed the *Herschel*/Photodetector Array Camera & Spectrometer (PACS; Pilbratt et al. 2010; Poglitsch et al. 2010) observations of SMM3 at 70 and 160 µm. Moreover, they used the *Herschel*/PACS 100 µm data from the HGBS. The aperture radii used for the photometry at the aforementioned three wavelengths were 9$''$6, 12$''$8, and 9$''$6, respectively, and the flux densities were found to be $S_{70\,\mu m} = 3.29 \pm 0.16$ Jy, $S_{100\,\mu m} = 10.91 \pm 2.79$ Jy, and $S_{160\,\mu m} = 16.94 \pm 2.54$ Jy (see Table 4 in S13). We note that the *Spitzer*/MIPS (the Multiband Imaging Photometer for *Spitzer*; Rieke et al. 2004) 70 µm flux density we determined in Paper I, 3.6 ± 0.4 Jy, is consistent with the aforementioned *Herschel*-based measurement (see Table 2 for the flux density comparison).

[8]http://www.submm.caltech.edu/~sharc/crush/index.htm.

Table 2 Mid-infrared to millimetre photometry of SMM3

Reference	$S_{24\,\mu m}$ [mJy]	$S_{70\,\mu m}$[a] [Jy]	$S_{100\,\mu m}$ [Jy]	$S_{160\,\mu m}$ [Jy]	$S_{350\,\mu m}$ [Jy]	$S_{870\,\mu m}$ [Jy]	$S_{2.9\,\mu m}$ [mJy]
This work	...	...	...	...	4.23 ± 1.30	1.58 ± 0.29	...
Paper I	5.0 ± 0.2	3.6 ± 0.4	...	...	...	2.5 ± 0.4	...
Paper III	...	...	...	...	5.4 ± 1.6	...	...
Stutz et al. (2013)	4.74 ± 0.3	3.29 ± 0.16	10.91 ± 2.79	16.94 ± 2.54	3.63[b]	$2.2/1.9$[c]	...
Tobin et al. (2015)	...	...	...	...	...	...	115.4 ± 3.9

Note: See the reference studies and text herein for details on how the tabulated flux densities were measured

[a]The 70 μm flux density from Paper I was measured using the *Spitzer*/MIPS data, while S13 used the *Herschel*/PACS data

[b]The authors adopted the SABOCA 350 μm peak surface brightness from Paper III

[c]The first value refers to a flux density measured in an aperture with radius equal to the beam FWHM (19″), while the latter one is otherwise the same but represents a background-subtracted value

3 Observational results

3.1 Images of continuum emission

In Fig. 1, we show the SABOCA and LABOCA submm images of SMM3, and *Spitzer* 4.5 μm and 24 μm images of the same region. We note that the latter two were retrieved from a set of Enhanced Imaging Products (SEIP) from the *Spitzer* Heritage Archive (SHA),[9] which include both the Infrared Array Camera (IRAC; Fazio et al. 2004) and MIPS Super Mosaics.

The LABOCA 870 μm dust continuum emission is slightly extended to the east of the centrally concentrated part of the core. From this eastern part the SABOCA 350 μm image reveals the presence of two subcondensations, designated SMM3b and 3c (Paper III). The *Spitzer* 24 μm image clearly shows that the core harbours a central protostar, while the 4.5 μm feature slightly east of the 24 μm peak is probably related to shock emission. In particular, the 4.5 μm band is sensitive to shock-excited H_2 and CO spectral line features (e.g. Smith and Rosen 2005; Ybarra and Lada 2009; De Buizer and Vacca 2010). As indicated by the plus signs in Fig. 1, our previous line observations probed the outer edge of SMM3, i.e. the envelope region. In contrast, the present single pointing line observations were made towards the 24 μm peak position. This positional difference has to be taken into account when comparing the chemical properties derived from our spectral line data.

3.2 Spectral line maps

In Fig. 2, we show the zeroth moment maps or integrated intensity maps of $DCO^+(3–2)$ and $p\text{-}H_2CO(3_{0,3}–2_{0,2})$ plotted as contours on the SABOCA 350 μm image. The

$DCO^+(3–2)$ map was constructed by integrating the line emission over the local standard of rest (LSR) velocity range of [7.4, 11.8] km s^{-1}. The $p\text{-}H_2CO(3_{0,3}–2_{0,2})$ line showed two velocity components. The line emission associated with SMM3 was integrated over [7.5, 11] km s^{-1}, while that of the lower-velocity component ($v_{LSR} \simeq 1.5$ km s^{-1}) was integrated over [−0.27, 2.49] km s^{-1}. The aforementioned velocity intervals were determined from the average spectra. The final 1σ noise levels in the zeroth moment maps were in the range 0.08–0.16 K km s^{-1} (on a T_{MB} scale).

With an offset of only $\Delta\alpha = -2\rlap{.}''6$, $\Delta\delta = 3\rlap{.}''3$, the $DCO^+(3–2)$ emission maximum is well coincident with the 350 μm peak position of the core. The corresponding offset from our new line observation target position is $\Delta\alpha = -1\rlap{.}''7$, $\Delta\delta = 5\rlap{.}''3$. Moreover, the emission is extended to the east (and slightly to the west), which resembles the dust emission morphology traced by LABOCA.

The $p\text{-}H_2CO(3_{0,3}–2_{0,2})$ emission, shown by black contours in Fig. 2, is even more elongated in the east-west direction than that of DCO^+. The emission peak is located inside the 7σ contour of $DCO^+(3–2)$ emission. We note that the 350 μm subcondensations SMM3b and 3c lie within the 3σ contour of both the line emissions.

The low-velocity component of $p\text{-}H_2CO(3_{0,3}–2_{0,2})$, with a radial velocity of about 1.5 km s^{-1}, is concentrated on the east and northeast parts of the mapped region. This is exactly where the $^{13}CO(2–1)$ and $C^{18}O(2–1)$ line emissions at $\sim$1.3 km s^{-1} were found to be concentrated (Miettinen 2012b). As discussed by Miettinen (2012b), several other high-density tracer lines at a radial velocity of 1.3–1.9 km s^{-1} have been detected towards other cores in Orion B9 (Papers I–III). Hence, the detection of $p\text{-}H_2CO(3_{0,3}–2_{0,2})$ emission at this low velocity comes as no surprise.
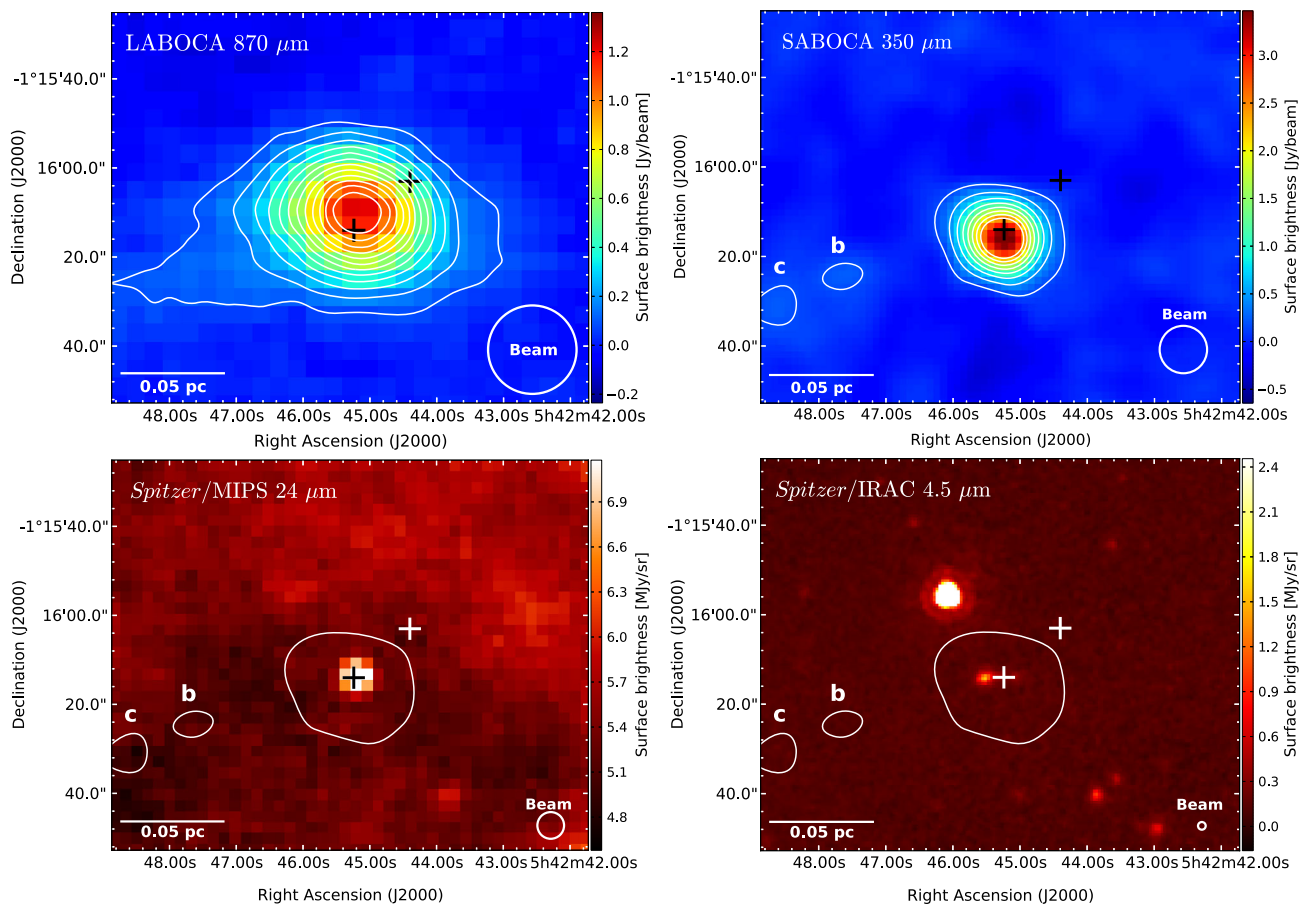
Fig. 1 Multiwavelength views of the SMM3 core. From *top left* to *bottom right* the panels show the LABOCA 870 μm, SABOCA 350 μm, *Spitzer*/MIPS 24 μm, and *Spitzer*/IRAC 4.5 μm images. The images are shown with linear scaling, and the *colour bars* indicate the surface-brightness scale in Jy beam^{-1} (APEX bolometers) or MJy sr^{-1} (*Spitzer*). The overlaid LABOCA contours in the *top left panel* start at 3σ, and increase in steps of 3σ, where $3\sigma = 90$ mJy beam^{-1}.

The SABOCA contours also start at 3σ, but increase in steps of 5σ ($1\sigma = 60$ mJy beam^{-1}). Both the *Spitzer* images are overlaid with the 3σ SABOCA contours. The positions of our molecular line observations are marked by *plus signs*. The 350 μm condensations, SMM3b and 3c, are also indicated. In the *bottom left corner of each panel*, a scale bar indicating the 0.05 pc projected length is shown. In the *bottom right corner of each panel*, the *circle* shows the beam size (HPBW)

3.3 Spectra and spectral line parameters

The previously observed spectra are shown in Fig. 3. The target position of these measurements is shown by the north-western plus sign in Figs. 1 and 2.

The new spectra, observed towards the 24 μm peak of SMM3, are presented in Fig. 4. The DCO$^+$(3–2) spectrum shown in the top panel of Fig. 4 was extracted from the line emission peak, and, as mentioned above, that position is well coincident with the 24 μm and 350 μm peaks (Fig. 2). The p-H$_2$CO($3_{0,3}$–$2_{0,2}$) line shown in Fig. 4 can be decomposed into two components, namely a narrow line at the systemic velocity, and a much broader one with non-Gaussian line-wing emission. The narrow line is probably originating in the quiescent envelope around the protostar, while the broad component is probably tracing the dense ambient gas swept up by an outflow (e.g. Yıldız et al. 2013). However, the mapped p-H$_2$CO($3_{0,3}$–$2_{0,2}$) data did not show

evidence of line wings (and hence we could not separately image the blue and redshifted parts of the line emission). The other two formaldehyde lines ($3_{2,1}$–$2_{2,0}$ and $3_{2,2}$–$2_{2,1}$) and the CH$_3$OH line shown in Fig. 4 are also broad, and hence likely originate in the swept-up outflow gas. A hint of an outflow wing emission is also visible in the SO spectrum.

Two velocity components are also seen in the ^{13}CO spectrum, one at the systemic velocity, and the other at ~ 1.5 km s^{-1}, the velocity at which p-H$_2$CO($3_{0,3}$–$2_{0,2}$) emission was seen in the line maps. The C^{18}O and ^{13}CO spectra exhibit absorption features next to the emission lines. These are caused by emission in the OFF beam positions when chopping between two positions on sky (wobbling secondary). This problem has been recognised in our previous papers on Orion B9, and is difficult to avoid when observing the abundant CO isotopologues. In fact, the detected ^{13}CO line at the systemic velocity suffers so badly
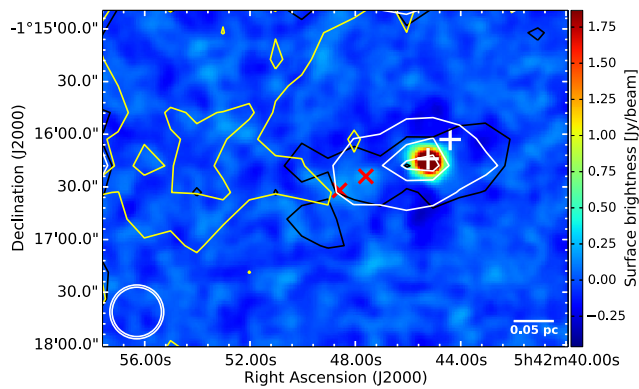
Fig. 2 Spectral line emission maps overlaid on the SABOCA 350 μm image. The DCO$^+$(3–2) emission is shown with *white contours* plotted at 3σ, 6σ, and 7σ (1σ = 0.16 K km s^{-1}). The *black contours* show the p-H$_2$CO(3$_{0,3}$–2$_{0,2}$) emission, plotted at 3σ and 5σ (1σ = 0.1 K km s^{-1}). The *yellow contours*, which show the low-velocity component of p-H$_2$CO(3$_{0,3}$–2$_{0,2}$), are drawn at 3σ and 6σ (1σ = 0.08 K km s^{-1}). The *white plus signs* mark our new and previous single-pointing line observation positions. The *red crosses* indicate the 350 μm peak positions of SMM3b and 3c (Paper III). The nested *circles* in the *bottom left corner* indicate the HPBW values of 28.″1 and 30.″7, i.e. the highest and coarsest resolutions of our new line observations (see Sect. 2). A *scale bar* indicating the 0.05 pc projected length is shown in the *bottom right corner*

from the subtraction of the off-signal that the line shape and intensity are deformed. For example, the intensity of the C^{18}O line appears to be higher than that of the more abundant ^{13}CO isotopologue. Hence, the ^{13}CO data are not used in the present study.

The hyperfine structure of the ammonia lines were fitted using the CLASS90's methods NH3(1, 1) and NH3(2, 2). The former method could be used to derive the optical thickness of the main hyperfine group (τ_m; see Sect. 4.2.1). The remaining lines shown in Fig. 3 are also split into hyperfine components, and hence were fitted using the CLASS90's hyperfine structure method.

Of the newly observed lines, only DCO$^+$(3–2) (cf. van der Tak et al. 2009) and ^{13}CO(2–1) (Cazzoli et al. 2004) exhibit hyperfine structure. In Fig. 4, the fits to the ^{13}CO lines are shown, but, as mentioned above, we do not study the lines further in the present paper. Single-Gaussian fits to the remaining lines were performed using CLASS90. The obtained line parameters are listed in Table 3. Columns (2)–(5) in this table give the LSR velocity (v_{LSR}), FWHM linewidth (Δv), peak intensity (T_{MB}), and the integrated line intensity ($\int T_{MB} dv$). Besides the formal 1σ fitting errors, the errors in the last two quantities also include the calibration uncertainty (15% for the Effelsberg/NH$_3$ data, and 10% for our APEX data). We note that rather than using a Gaussian fit, the integrated intensity of the C^{17}O line was computed by integrating over the velocity range [5.87, 10.14] km s^{-1} to take the non-Gaussian shape of the line into account.
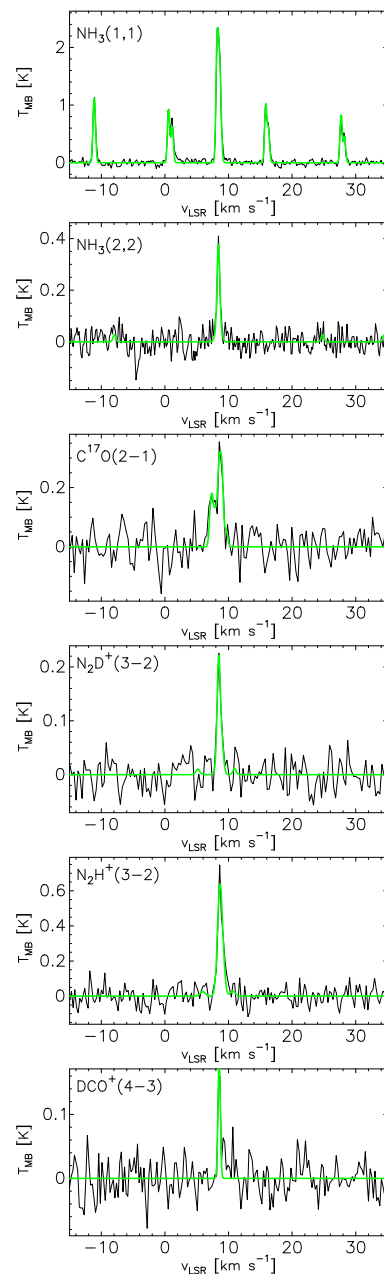

Fig. 3 Hanning-smoothed spectra originally published in Papers II and III. The hyperfine structure fits are shown with *green lines*. The velocity range shown in all panels was chosen so that the outer p-NH$_3$(1, 1) satellite *lines* can be seen

4 Analysis and results

4.1 Spectral energy distribution of SMM3—modified blackbody fitting

The SED of SMM3, constructed using the *Herschel*/PACS 70, 100, and 160 μm, SABOCA 350 μm, LABOCA 870 μm, and CARMA 2.9 mm flux densities (see Sects. 2.3 and 2.4, and Table 2), is show in Fig. 5. The *Spitzer* 24 μm data point, which represents a flux density of 4.74 ± 0.3 mJy from S13,
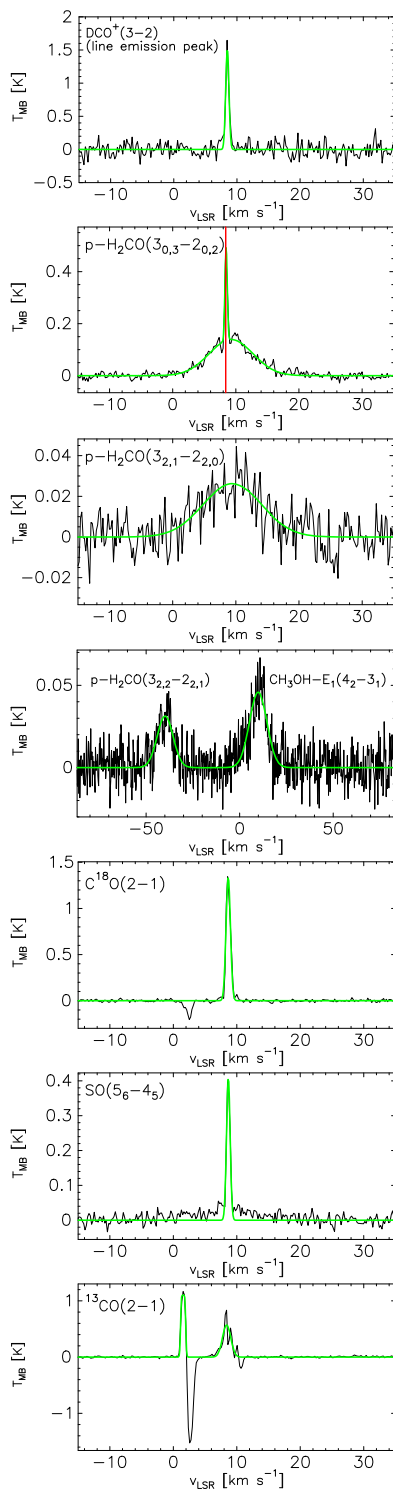
Fig. 4 Hanning-smoothed spectra obtained with our new APEX observations. The DCO$^+$(3–2) spectrum was extracted from the line emission peak. The single-Gaussian fits are shown with *green lines*, while those overlaid on the DCO$^+$ and ^{13}CO spectra show the hyperfine structure fits. The p-H$_2$CO($3_{0,3}$–$2_{0,2}$) and ^{13}CO spectra show two velocity components. The *red vertical line* plotted on the former spectrum indicates the radial velocity of the p-NH$_3$(1, 1) line. The velocity range is wider in the *fourth panel from top* to show the two nearby *lines*. The features with negative intensity in the C^{18}O and ^{13}CO spectra are caused by emission in the observed OFF position

is also shown in the figure, but it was excluded from the fit (see below). We note that the S13 24 μm flux density is close to a value of 5.0 ± 0.2 mJy we determined in Paper I (13″ aperture; see Table 2). The 24 μm emission originates in a warmer dust component closer to the accreting central protostar, while the longer wavelength data ($\lambda \geq 70$ μm) are presumable tracing the colder envelope.

The solid line in Fig. 5 represents a single-temperature MBB function fitted to the aforementioned data points. The fit was accomplished with optimisation (χ^2 minimisation) by simulated annealing (Kirkpatrick et al. 1983), which, although more time-consuming, can work better in finding the best fit solution than the most commonly-used standard (non-linear) least-squares fitting method that can be sensitive to the chosen initial values (see also Bertsimas and Tsitsiklis 1993; Ireland 2007). The original version of the fitting algorithm was written by J. Steinacker (M. Hennemann, priv. comm.). It was assumed that the thermal dust emission is optically thin ($\tau \ll 1$). We note that this assumption is probably good for the wavelengths longward of 70 μm, but it gets worse at shorter wavelengths. This, together with the fact that 24 μm emission originates in a warmer dust component closer to the accreting central protostar than the longer wavelength emission ($\lambda \geq 70$ μm) arising from the colder envelope, is the reason why we excluded the 24 μm flux density from the fit (e.g. Ragan et al. 2012). The model fit takes into account the wavelength-dependence of the dust opacity (κ_λ). As the dust model, we employed the widely used Ossenkopf and Henning (1994, hereafter OH94) model describing graphite-silicate dust grains that have coagulated and accreted thin ice mantles over a period of 10^5 yr at a gas density of 10^5 cm^{-3}. For the total dust-to-gas mass ratio we adopted a value of $\delta_{\rm dg} \equiv M_{\rm dust}/M_{\rm gas} = 1/141$. This mass ratio is based on the assumption that the core's chemical composition is similar to the solar mixture, i.e. the mass fractions for hydrogen, helium, and heavier elements were assumed to be $X = 0.71$, $Y = 0.27$, and $Z = 0.02$, respectively.[10]

As can be seen in Fig. 5, the PACS data are reasonably well fitted although the 160 μm flux density is slightly overestimated. The SABOCA data point is not well fitted, which could be partly caused by the spatial filtering owing to the sky-noise removal. Hence, a ground-based bolometer flux density can appear lower than what would be expected from the *Herschel* data. On the other hand, our LABOCA data point is well matched with the MBB fit. Finally, we note that the CARMA 2.9 mm flux density, which is based on the highest angular resolution data used here, is underestimated by the MBB curve. Radio continuum observations would be needed to quantify the amount of free-free contribution at 2.9 mm (cf. Ward-Thompson et al. 2011).

---

[10]In this case, the ratio between the total mass (H+He+metals) to hydrogen mass is $1/X \simeq 1.41$.

Table 3 Spectral line parameters

Transition	v_{LSR} [km s^{-1}]	Δv [km s^{-1}]	T_{MB} [K]	$\int T_{MB} dv$ [K km s^{-1}]	τ	T_{ex} [K]	T_{rot} [K]
p-NH$_3$(1, 1)	8.40 ± 0.01	0.40 ± 0.01	2.46 ± 0.40[a]	1.91 ± 0.30[a]	$2.01 \pm 0.11 (= \tau_m)$[a]	6.8 ± 0.7	10.6 ± 0.5
p-NH$_3$(2, 2)	8.42 ± 0.02	0.45 ± 0.08	0.37 ± 0.06[a]	0.23 ± 0.04[a]	$0.10 \pm 0.02 (= \tau_0)$[b]	6.8 ± 0.7[c]	...
DCO$^+$(3–2)[d]	8.48 ± 0.02	0.60 ± 0.04	1.51 ± 0.19	0.98 ± 0.11	$0.84 \pm 0.30 (= \tau_0)$[e]	6.8 ± 0.7[f]	...
p-H$_2$CO($3_{0,3}$–$2_{0,2}$)[g]	8.46 ± 0.01	0.42 ± 0.02	0.38 ± 0.04	0.17 ± 0.02	$0.06 \pm 0.01 (= \tau_0)$[h]	11.2 ± 0.5[h]	...
	9.26 ± 0.08	8.22 ± 0.21	0.14 ± 0.02	1.21 ± 0.12	$\ll 1$[i]	...	64 ± 15[i]
CH$_3$OH-E$_1$($4_{2,2}$–$3_{1,2}$)	9.93 ± 0.29	10.98 ± 0.80	0.05 ± 0.01	0.54 ± 0.06	$0.0009 \pm 0.0002 (= \tau_0)$[j]	64 ± 15[j]	...
p-H$_2$CO($3_{2,2}$–$2_{2,1}$)	8.99 ± 0.47	10.07 ± 1.23	0.03 ± 0.01	0.34 ± 0.05	$\ll 1$[i]	...	64 ± 15[i]
p-H$_2$CO($3_{2,1}$–$2_{2,0}$)	9.45 ± 0.35	10.92 ± 0.83	0.03 ± 0.01	0.31 ± 0.04	$\ll 1$[i]	...	64 ± 15[i]
C^{18}O(2–1)	8.66 ± 0.01	0.82 ± 0.01	1.33 ± 0.16	1.17 ± 0.12	$0.23 \pm 0.02 (= \tau_0)$[k]	11.2 ± 0.5[k]	...
SO(5_6–4_5)	8.67 ± 0.01	0.68 ± 0.02	0.41 ± 0.05	0.29 ± 0.03	$0.06 \pm 0.01 (= \tau_0)$[k]	11.2 ± 0.5[k]	...
^{13}CO(2–1)[g]	8.38 ± 0.15	1.51 ± 0.35	0.57 ± 0.18	0.93 ± 0.27	...	...	...
	1.53 ± 0.03	0.43 ± 0.03	1.32 ± 0.26	0.89 ± 0.15	...	...	...
C^{17}O(2–1)	8.68 ± 0.06	0.59 ± 0.11	0.34 ± 0.05	0.54 ± 0.07	$0.05 \pm 0.01 (= \tau_0)$[k]	11.2 ± 0.5[k]	...
N$_2$D$^+$(3–2)	8.39 ± 0.04	0.53 ± 0.11	0.21 ± 0.03	0.17 ± 0.03	$0.09 \pm 0.02 (= \tau_0)$[l]	6.8 ± 0.7[f]	...
N$_2$H$^+$(3–2)	8.57 ± 0.03	0.85 ± 0.09	0.62 ± 0.10	0.67 ± 0.08	$0.36 \pm 0.11 (= \tau_0)$[l]	6.8 ± 0.7[f]	...
DCO$^+$(4–3)	8.54 ± 0.03	0.42 ± 0.18	0.20 ± 0.02	0.09 ± 0.02	$0.11 \pm 0.03 (= \tau_0)$[e]	6.8 ± 0.7[f]	...

The parameters given in columns (2)–(5) are described in Sect. 3.3, while those in the last three columns are the line optical thickness, excitation temperature, and rotational temperature (Sect. 4.2.1)

[a]These values refer to the main group of hyperfine components ($F_1 = 1$–1 and $F_1 = 2$–2 for the $(J, K) = (1, 1)$ transition; $F_1 = 1$–1, $F_1 = 2$–2, and $F_1 = 3$–3 for the $(J, K) = (2, 2)$ transition). The total NH$_3$(1, 1) line optical thickness is twice the main group value, i.e. $\tau_{tot} = 2\tau_m$

[b]Peak optical thickness of the strongest hyperfine component ($F = 7/2$–7/2, $F_1 = 3$–3; weight 8/35) calculated using T_{ex}[NH$_3$(1, 1)]

[c]Assumed to be that of the NH$_3$(1, 1) transition

[d]The analysed beam-averaged spectrum was extracted from the line emission peak

[e]The value of τ_0 refers to the strongest hyperfine component, which is $F = 4$–3 for $J = 3$–2 (relative intensity R.I. $= 3/7$), and $F = 5$–4 for $J = 4$–3 (R.I. $= 11/27$)

[f]The value of T_{ex} was assumed to be that derived for NH$_3$(1, 1), and the value of τ_0 was calculated based on this assumption

[g]Two velocity components were detected. The ^{13}CO lines are not analysed further in the present work (Sect. 3.3)

[h]The narrow line component at the systemic velocity was assumed to be thermalised at the kinetic temperature (T_{kin}) derived from NH$_3$. The peak optical thickness was then calculated under the assumption that $T_{ex} = T_{kin}$

[i]A rotational diagram method was used to derive T_{rot}, under the assumption of optically thin emission

[j]The value of T_{ex} was assumed to be equal to $T_{rot}(p$–H$_2$CO), and τ_0 was estimated accordingly

[k]The line was assumed to be thermalised at T_{kin}(NH$_3$), and τ_0 was calculated under this assumption. For C^{17}O, the relative intensity of the strongest hyperfine component $F = 9/2$–7/2 is R.I. $= 1/3$

[l]The value of τ_0 refers to the strongest hyperfine component, i.e. $J_{F_1 F} = 3_{45}$–2_{34} for both N$_2$H$^+$ and N$_2$D$^+$ (R.I. $= 11/63$)

The dust temperature, envelope mass, and luminosity obtained from the SED fit are $T_{dust} = 15.1 \pm 0.1$ K, $M_{env} = 3.1 \pm 0.6$ M$_\odot$, and $L = 3.8 \pm 0.6$ L$_\odot$. However, we emphasise that these values should be taken with some caution because clearly the fit shown in Fig. 5 is not perfect. In principle, while the 24 μm emission is expected to trace a warmer dust component than those probed by $\lambda_{obs} \geq 70$ μm observations (e.g. Ragan et al. 2012), it is possible that our poor single-T_{dust} fit reflects the presence of more than one cold dust components in the protostar's envelope, and would hence require a multi-T_{dust} fit. However, following S13, and to allow an easier comparison with their results, we opt to use a simplified single-T_{dust} MBB in the present study.

We note that $M_{env} \propto (\kappa_\lambda \delta_{dg})^{-1}$, and hence the choice of the dust model (effectively κ_λ) and δ_{dg} mostly affect the envelope mass among the SED parameters derived here (by a factor of two or more; OH94). The adopted dust model can also (slightly) influence the derived values of T_{dust} and L
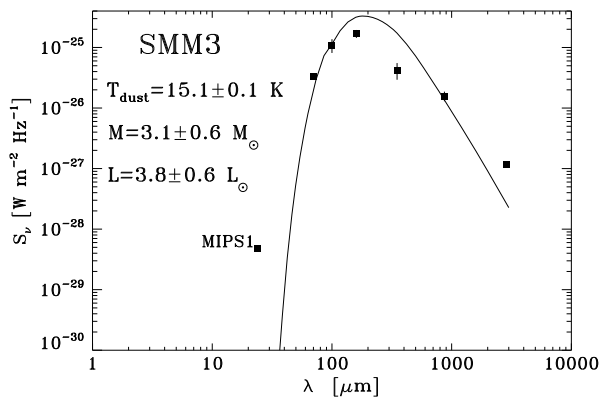
Fig. 5 Spectral energy distribution of SMM3. The *square symbols with vertical error bars* represent the measured flux densities (*Herschel*/PACS, SABOCA, LABOCA, and CARMA). A modified blackbody fit to the data points is shown by a *solid black line*. The *Spitzer* 24 μm data point from S13 is also indicated (MIPS1), but not used in the fit

because of the varying dust emissivity index (β) among the different OH94 models ($\kappa_\lambda \propto \lambda^{-\beta}$). The submm luminosity, L_{submm}, computed by numerically integrating the fitted SED curve longward of 350 μm, is about 0.23 $L_\odot$, i.e. about 6% of the total luminosity. For Class 0 protostellar cores, the L_{submm}/L ratio is defined to be $> 5 \times 10^{-3}$, which reflects the condition that the envelope mass exceeds that of the central protostar, i.e. $M_{\mathrm{env}} \gg M_\star$ (André et al. 1993, 2000). With a L_{submm}/L ratio of about one order of magnitude higher than the definition limit, SMM3 is clearly in the Class 0 regime.

Our T_{dust} value is by a factor of 1.4 lower than that obtained by S13 through their MBB analysis, while the values of M_{env} and L we derived are higher by factors of about 9.4 and 1.8, respectively (see Sect. 1). We note that similarly to the present work, S13 fitted the data at $\lambda \geq 70$ μm, but they adopted a slightly different OH94 dust model (coagulation at a density of 10^6 cm^{-3} rather than at 10^5 cm^{-3} as here), and a slightly higher gas-to-dust ratio than we ($1.36 \times 110 = 149.6$, which is 6% higher than our value of 141). Hence, we attribute the aforementioned discrepancies to the different SABOCA and LABOCA flux density values used in the analysis (e.g. S13 used the peak surface brightness from our SABOCA map, and their fit underestimated the LABOCA flux density), and to the fact that we have here used the new CARMA 2.9 mm data from Tobin et al. (2015) as well.

Given that Class 0 objects have, by definition, $M_{\mathrm{env}} \gg M_\star$, an envelope mass of ~3 $M_\odot$ derived here might be closer to the true value than a value of ~0.3 $M_\odot$ derived by S13. Also, as was already mentioned in Sect. 1, SMM3 was found to be a very bright 2.9 mm-emitter by Tobin et al. (2015), and hence they derived a high mass of 7.0 ± 0.7 $M_\odot$ under the assumption that $T_{\mathrm{dust}} = 20$ K and $\delta_{\mathrm{dg}} = 1/100$

(their mass is 2.3 ± 0.5 times higher than the present estimate, but a direct comparison with a single-flux density analysis is not feasible). In the context of stellar evolution, if the core star formation efficiency is $\sim30\%$ (e.g. Alves et al. 2007), and the central SMM3 protostar has $M_\star \ll M_{\mathrm{env}}$, this source could evolve into a near solar-mass star if $M_{\mathrm{env}} \sim 3$ $M_\odot$ as estimated here, while an envelope mass of ~0.3 $M_\odot$ would only be sufficient to form a very low-mass single star (near the substellar–stellar limit of ~0.1 $M_\odot$). Moreover, the dust temperature we have derived here is closer to the gas kinetic temperature in SMM3 (the ratio between the two is 1.35 ± 0.06; see Sect. 4.2.1) than the value $T_{\mathrm{dust}} = 21.4 \pm 0.4$ K from S13. In a high-density protostellar envelope, the gas temperature is indeed expected to be similar to T_{dust} (e.g. the dust–gas coupling occurs at $\sim10^5$ cm^{-3} in the Hollenbach and McKee 1989 prescription). Finally, the physical implication of the higher luminosity we have derived here—1.8 ± 0.3 times the S13 value—is that the mass accretion rate of the SMM3 protostar is higher by a similar factor.

4.2 Analysis of the spectral line data

4.2.1 Line optical thicknesses, and the excitation, rotational, and kinetic temperatures

The optical thickness of the main p-NH$_3$(1, 1) hyperfine group, τ_{m}, could be derived by fitting the hyperfine structure of the line. The main hyperfine group ($\Delta F = 0$) has a relative strength of half the total value, and hence the total optical thickness of p-NH$_3$(1, 1) is given by $\tau_{\mathrm{tot}} = 2\tau_{\mathrm{m}}$ ($= 2 \times (2.01 \pm 0.11)$; see Mangum et al. 1992; Appendix A1 therein). The strongest hyperfine component has a relative strength of 7/30, which corresponds to a peak optical thickness of $\tau_0 \simeq 0.94$. The excitation temperature of the line, T_{ex}, was calculated from the antenna equation ($T_{\mathrm{MB}} \propto (1 - e^{-\tau})$; see e.g. Eq. (1) in Paper I), assuming that the background temperature is equal to that of the cosmic microwave background radiation, i.e. $T_{\mathrm{bg}} \equiv T_{\mathrm{CMB}} = 2.725$ K (Fixsen 2009). The obtained value, $T_{\mathrm{ex}} = 6.8 \pm 0.7$ K,[11] was also adopted for the p-NH$_3$(2, 2) line because its hyperfine satellites were not detected. Using this assumption and the antenna equation, the peak p-NH$_3$(2, 2) optical thickness was determined to be 0.1 ± 0.02. To calculate τ_{tot}, this value should be scaled by the relative strength of the strongest hyperfine component which is 8/35. The value $T_{\mathrm{ex}} = 6.8 \pm 0.7$ K was also adopted for the N$_2$H$^+$, N$_2$D$^+$, and DCO$^+$ lines, although we note that they might originate in a denser gas than the observed ammonia lines. Another caveat is that the $J = 3$–2 line of DCO$^+$ was extracted from

---

[11] We note that in Paper II we determined a value of T_{ex}(NH$_3$) $= 6.1 \pm 0.5$ K from a unsmoothed p-NH$_3$(1, 1) spectrum, while the present value was derived from a smoothed spectrum.

a position different from the ammonia target position, but, within the errors, the aforementioned T_{ex} value is expected to be a reasonable choice (e.g. Anderson et al. 1999). The values of τ_0 were then derived as in the case of the (2, 2) transition of ammonia (see Col. (6) in Table 3).

Using the $\tau_m[p-NH_3(1, 1)]$ value and the intensity ratio between the (2, 2) and (1, 1) lines of p-NH$_3$, we derived the rotational temperature of ammonia (T_{rot}; see Eq. (4) in Ho et al. 1979). This calculation assumed that the T_{ex} values, and also the linewidths, are equal between the two inversion lines. The latter assumption is justified by the observed FWHM linewidths. The derived value of T_{rot}, 10.6 ± 0.5 K, was converted into an estimate of the gas kinetic temperature using the $T_{kin} - T_{rot}$ relationship from Tafalla et al. (2004; their Appendix B), which is valid in the low-temperature regime of $T_{kin} \in [5, 20]$ K. The value we derived, $T_{kin} = 11.2 \pm 0.5$ K,[12] was adopted as T_{ex} for the observed CO isotopologue transitions, SO, and the narrow p-H$_2$CO line. The choice of $T_{ex} = T_{kin}$ means that the level populations are assumed to be thermalised, and this is often done in the case of C^{18}O (e.g. Hacar and Tafalla 2011), while in the cases of SO and H$_2$CO it should be taken as a rough estimate only.

The three broad p-H$_2$CO lines we detected allowed us to construct a rotational diagram for p-H$_2$CO. The rotational diagram technique is well established, and details of the method can be found in a number of papers (e.g. Linke et al. 1979; Turner 1991; Goldsmith and Langer 1999; Anderson et al. 1999; Green et al. 2013). When the line emission is assumed to be optically thin, the integrated intensity of the line is related to T_{rot} and the total column density of the species, N, according to the equation

$$\ln\left[\frac{\int T_{MB} dv}{\nu S g_K g_I}\right] = \ln\left(\frac{2\pi^2 \mu^2}{3k_B\epsilon_0}\frac{N}{Z_{rot}}\right) - \frac{1}{T_{rot}}\frac{E_u}{k_B}, \quad (1)$$

where S is the line strength, g_K is the K-level degeneracy, g_I is the reduced nuclear spin degeneracy, ϵ_0 is the vacuum permittivity, and Z_{rot} is the rotational partition function. The values of S were adopted from the Splatalogue database.[13] Because H$_2$CO is an asymmetric top molecule, there is no K-level degeneracy, and hence $g_K = 1$. For the *para* form of H$_2$CO (K_a is even), the value of g_I is 1/4 (Turner 1991). The H$_2$CO molecule belongs to a C_{2v} symmetry group (two vertical mirror planes), and its partition function at the high-temperature limit ($hA/k_BT_{ex} \ll 1$, where h is the Planck constant) can be approximated as (Turner 1991)

$$Z_{rot}(T_{rot}) \simeq \frac{1}{2}\sqrt{\frac{\pi(k_BT_{rot})^3}{h^3 ABC}}. \quad (2)$$

---

[12]The quoted value of T_{kin} differs slightly from the one derived in Paper II (11.3 ± 0.8 K) because of the smoothed ammonia spectra employed in the analysis in the present work.
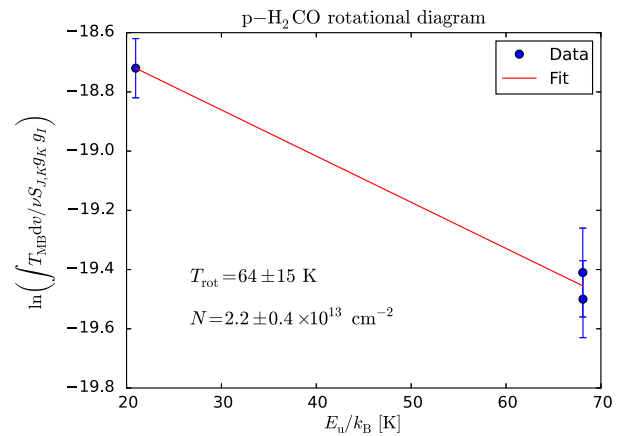
[13]http://www.cv.nrao.edu/php/splat/.

Fig. 6 Rotational diagram for p-H$_2$CO. The left-hand side of Eq. (1) is plotted as a function of the energy of the upper level. The *red solid line* shows a least-squares fit to the observed data. The resulting values of T_{rot} and N are indicated

The derived rotational diagram, i.e. the left-hand side of Eq. (1) plotted as a function of E_u/k_B, is shown in Fig. 6. The red solid line represents a least-squares fit to the three data points. The fit provides a value of T_{rot} as the reciprocal of the slope of the line, and N can be calculated from the y-intercept. We note that two of the detected p-H$_2$CO transitions have almost the same upper-state energy, i.e. they lie very close to each other in the direction of the x-axis in Fig. 6, which makes the fitting results rather poorly constrained. We also note that the *ortho*-H$_2$CO($2_{1,1}$–$1_{1,1}$) line detected by Kang et al. (2015) refers to the narrow-line component ($\Delta v = 0.45$ km s^{-1}), and hence cannot be employed in our rotational diagram for the broad-line component. The value of T_{rot} we derived is 64 ± 15 K, which in the case of local thermodynamic equilibrium (LTE) is equal to T_{kin}. Owing to the common formation route for formaldehyde and methanol (Sect. 5.2.3), the aforementioned T_{rot} value was adopted as T_{ex} for the detected CH$_3$OH line (which then appears to be optically thin). The molecular column density calculations are described in the next subsection.

4.2.2 Molecular column densities and fractional abundances

As described above, the beam-averaged column density of p-H$_2$CO for the broad component was derived using the rotational diagram method. The column densities of the species other than NH$_3$ (see below) were calculated by using the standard LTE formulation

$$N = \frac{3h\epsilon_0}{2\pi^2}\frac{1}{\mu^2 S}\frac{Z_{rot}(T_{ex})}{g_K g_I}e^{E_u/k_B T_{ex}}F(T_{ex})\int \tau(v)dv, \quad (3)$$

where $F(T_{ex}) \equiv (e^{h\nu/k_B T_{ex}} - 1)^{-1}$. Here, the electric dipole moment matrix element is defined as $|\mu_{ul}| \equiv \mu^2 S/g_u$, where $g_u \equiv g_J = 2J + 1$ is the rotational degeneracy of the upper

state (Townes and Schawlow 1975). The values of the product $\mu^2 S$ were taken from the Splatalogue database, but we note that for linear molecules S is simply equal to the rotational quantum number of the upper state, i.e. $S = J$ (the SO molecule, which possesses a $^3\Sigma$ (electronic spin is 1) electronic ground state, is an exception; Tiemann 1974). For linear molecules, $g_K = g_I = 1$ for all levels, while for the E-type CH_3OH, $g_K = 2$ and $g_I = 1$ (Turner 1991).

The partition function of the linear molecules was approximated as

$$Z_{rot}(T_{ex}) \simeq \frac{k_B T_{ex}}{hB} + \frac{1}{3}. \tag{4}$$

Equation (4) is appropriate for heteropolar molecules at a high-temperature limit of $hB/k_B T_{ex} \ll 1$. For SO, however, the rotational levels with $N \geq 1$ are split into three sublevels (triplet of $N = J - 1$, $N = J$, and $N = J + 1$). To calculate the partition function of SO, we used the approximation formulae from Kontinen et al. (2000; Appendix A therein). For CH_3OH, which has an internal rotor, the partition function is otherwise similar to that in Eq. (2) but with a numerical factor of 2 instead of 1/2 (Turner 1991).

When the spectral line has a Gaussian profile, the last integral term in Eq. (3) can be expressed as a function of the FWHM linewidth and peak optical thickness of the line as

$$\int \tau(v)dv = \frac{\sqrt{\pi}}{2\sqrt{\ln 2}} \Delta v \tau_0 \simeq 1.064 \Delta v \tau_0. \tag{5}$$

We note that for the lines with hyperfine structure the total optical thickness is the sum of peak optical thicknesses of the different components. Moreover, if the line emission is optically thin ($\tau \ll 1$), $T_{MB} \propto \tau$, and N can be computed from the integrated line intensity. The values of τ listed in Col. (6) in Table 3 were used to decide whether the assumption of optically thin emission is valid (in which case the column density was calculated from the integrated intensity).

To derive the total column density of NH_3, we first calculated that in the (1, 1) state, which, by taking into account both parity states of the level, is given by (e.g. Harju et al. 1993)

$$N(NH_3)_{(1, 1)} = N_+ + N_- = N_+ \left(1 + e^{h\nu_{(1, 1)}/k_B T_{ex}}\right). \tag{6}$$

The latter equality follows from the Boltzmann population distribution, and the fact that the two levels have the same statistical weights (J and K do not change in the inversion transition). Because N_+ represents the column density in the upper state, its value was calculated from a formula that can be derived by substituting Eq. (5) into Eq. (3), and dividing by the term $Z_{rot}/(g_K g_I)e^{E_u/k_B T_{ex}}$. The value of S for a $(J, K) \rightarrow (J, K)$ transition is $S = K^2/[J(J + 1)]$. Finally, making the assumption that at the low temperature of SMM3 only the four lowest metastable ($J = K$) levels are

populated, the value of $N(NH_3)_{(1, 1)}$ was scaled by the partition function ratio $Z_{rot}/Z_{rot}(1, 1)$ to derive the total (ortho+para) NH_3 column density as

$$N(NH_3) = N(NH_3)_{(0, 0)} + N(NH_3)_{(1, 1)}$$
$$+ N(NH_3)_{(2, 2)} + N(NH_3)_{(3, 3)}$$
$$= N(NH_3)_{(1, 1)}$$
$$\times \left(\frac{1}{3}e^{\frac{23.4}{T_{rot}}} + 1 + \frac{5}{3}e^{-\frac{41.5}{T_{rot}}} + \frac{14}{3}e^{-\frac{101.2}{T_{rot}}}\right). \tag{7}$$

The column density analysis presented here assumes that the line emission fills the telescope beam, i.e. that the beam filling factor is unity. As can be seen in Fig. 2, the $DCO^+(3-2)$ and $p\text{-}H_2CO(3_{0, 3}-2_{0, 2})$ emissions are somewhat extended with respect to the 350 μm-emitting core whose size is comparable to the beam size of most of our line observations. Moreover, the detected N-bearing species are often found to show spatial distributions comparable to the dust emission of dense cores (e.g. Caselli et al. 2002a; Lai et al. 2003; Daniel et al. 2013). It is still possible, however, that the assumption of unity filling factor is not correct. The gas within the beam area can be structured in a clumpy fashion, in which case the true filling factor is <1. The derived beam-averaged column density is then only a lower limit to the source-averaged value.

The fractional abundances of the molecules were calculated by dividing the molecular column density by the H_2 column density, $x = N/N(H_2)$. To be directly comparable to the molecular line data, the $N(H_2)$ values were derived from the LABOCA data smoothed to the resolution of the line observations (cf. Eq. (3) in Paper I). For this calculation, we adopted the dust temperature derived from the SED fit ($T_{dust} = 15.1 \pm 0.1$ K), except for the broad component of $p\text{-}H_2CO$ and CH_3OH for which T_{dust} was assumed to be 64 ± 15 K (= $T_{rot}(p - H_2CO)$). The mean molecular weight per H_2 molecule we used was $\mu_{H_2} = 2.82$, and the dust opacity per unit dust mass at 870 μm was set to $\kappa_{870\,\mu m} = 1.38\ cm^2\ g^{-1}$ to be consistent with the OH94 dust model described earlier. The beam-averaged column densities and abundances with respect to H_2 are listed in Table 4.

4.2.3 Deuterium fractionation and CO depletion

The degree of deuterium fractionation in N_2H^+ was calculated by dividing the column density of N_2D^+ by that of N_2H^+. The obtained value, $14\% \pm 6\%$, is about 40% of the value derived in Paper III (i.e. 0.338 ± 0.09 based on a non-LTE analysis).

To estimate the amount by which the CO molecules are depleted in SMM3, we calculated the CO depletion factors following the analysis presented in Paper III with the following modifications. Recently, Ripple et al. (2013) analysed the CO abundance variation across the Orion giant

Table 4 Molecular column densities, fractional abundances with respect to H_2, and the degrees of deuteration and CO depletion

Species	N [cm^{-2}]	x
NH_3	$1.5 \pm 0.2 \times 10^{15}$	$6.6 \pm 0.9 \times 10^{-8}$
$p\text{-}H_2CO$[a]	$1.0 \pm 0.3 \times 10^{12}$	$2.0 \pm 0.6 \times 10^{-11}$
$p\text{-}H_2CO$[b]	$2.2 \pm 0.4 \times 10^{13}$	$3.1 \pm 1.0 \times 10^{-9}$
CH_3OH	6.8×10^{14}[c]	$9.4 \pm 2.5 \times 10^{-8}$
$C^{18}O$	$7.1 \pm 0.8 \times 10^{14}$	$1.5 \pm 0.1 \times 10^{-8}$
SO	$8.1 \pm 1.2 \times 10^{12}$	$1.6 \pm 0.2 \times 10^{-10}$
$C^{17}O$	$3.2 \pm 0.4 \times 10^{14}$	$1.2 \pm 0.1 \times 10^{-8}$
N_2D^+	$1.7 \pm 0.5 \times 10^{12}$	$4.8 \pm 1.4 \times 10^{-11}$
N_2H^+	$1.2 \pm 0.4 \times 10^{13}$	$2.9 \pm 0.9 \times 10^{-10}$
DCO^+[d]	$1.3 \pm 0.5 \times 10^{13}$	$2.6 \pm 1.0 \times 10^{-10}$
DCO^+[e]	$6.2 \pm 2.9 \times 10^{11}$	$2.0 \pm 0.9 \times 10^{-11}$
	Core centre	Envelope
$[N_2D^+]/[N_2H^+]$	…	0.14 ± 0.06
$f_D(CO)$	27.3 ± 1.8	8.3 ± 0.7

[a]The narrow-line component, which likely originates in the quiescent envelope

[b]The broad-line/warm component, which likely originates in the outflow gas

[c]The estimated error is unrealistically large (much larger than the nominal value), and is therefore not reported

[d]From the $J = 3$–2 line observation towards the core centre

[e]From the previous $J = 4$–3 line observation towards the core envelope

molecular clouds. In particular, they derived the ^{13}CO fractional abundances, and found that in the self-shielded interiors ($3 < A_V < 10$ mag) of Orion B, the value of $x(^{13}CO)$ is $\simeq 3.4 \times 10^{-6}$. On the other hand, towards NGC 2024 in Orion B the average $[^{12}C]/[^{13}C]$ ratio is measured to be about 68 (Savage et al. 2002; Milam et al. 2005). These two values translate into a canonical (or undepleted) CO abundance of $\simeq 2.3 \times 10^{-4}$. We note that this is 2.3 times higher than the classic value 10^{-4}, but fully consistent with the best-fitting CO abundance of $2.7^{+6.4}_{-1.2} \times 10^{-4}$ found by Lacy et al. (1994) towards NGC 2024. Because we derived the $C^{18}O$ and $C^{17}O$ abundances towards the core centre and the envelope, respectively, the canonical abundances of these two species had to be estimated. We assumed that the $[^{16}O]/[^{18}O]$ ratio is equal to the average local interstellar medium value of 557 (Wilson 1999), and that the $[^{18}O]/[^{17}O]$ ratio is that derived by Wouterloot et al. (2008) for the Galactic disk (Galactocentric distance range of 4–11 kpc), namely 4.16. Based on the aforementioned ratios, the canonical $C^{18}O$ and $C^{17}O$ abundances were set to 4.1×10^{-7} and 9.9×10^{-8}, respectively. With respect to the observed abundances, the CO depletion factors were derived to be $f_D = 27.3 \pm 1.8$ towards the core centre ($C^{18}O$ data), and $f_D = 8.3 \pm 0.7$ in the envelope ($C^{17}O$ data). The deuter-

ation level and the CO depletion factors are given in the last two rows in Table 4. We note that the non-LTE analysis presented in Paper III yielded a value of $f_D = 10.8 \pm 2.2$ towards the core edge, i.e. a factor of 1.3 ± 0.3 times higher than the present value.

Assuming that the core mass we derived through SED fitting, 3.1 ± 0.6 M$_\odot$, is the mass within an effective radius, which corresponds to the size of the largest photometric aperture used, i.e. $R_{\text{eff}} = 19.''86$ or $\simeq 0.04$ pc, the volume-averaged H_2 number density is estimated to be $\langle n(H_2) \rangle = 1.7 \pm 0.3 \times 10^5$ cm^{-3} (see Eq. (1) in Paper III). Following the analysis presented in Miettinen (2012a, Sect. 5.5 therein), the CO depletion timescale at the aforementioned density (and adopting a δ_{dg} ratio of 1/141) is estimated to be $\tau_{\text{dep}} \sim 3.4 \pm 0.6 \times 10^4$ yr. This can be interpreted as a lower limit to the age of SMM3.

5 Discussion

5.1 Fragmentation and protostellar activity in SMM3

Owing to the revised fundamental physical properties of SMM3, we are in a position to re-investigate its fragmentation characteristics. At a gas temperature of $T_{\text{kin}} = 11.2 \pm 0.5$ K, the isothermal sound speed is $c_s = 197.5 \pm 4.4$ m s^{-1}, where the mean molecular weight per free particle was set to $\mu_p = 2.37$. The aforementioned values can be used to calculate the thermal Jeans length

$$\lambda_J = \sqrt{\frac{\pi c_s^2}{G \langle \rho \rangle}}, \tag{8}$$

where G is the gravitational constant, the mean mass density is $\langle \rho \rangle = \mu_{H_2} m_H \langle n(H_2) \rangle$, and m_H is the mass of the hydrogen atom. The resulting Jeans length, $\lambda_J \simeq 0.05$ pc, is a factor of 1.4 shorter than our previous estimate (0.07 pc; Paper III), where the difference can be mainly attributed to the higher gas density derived here. We note that the uncertainty propagated from those of T_{kin} and $\langle n(H_2) \rangle$ is only 1 mpc.

If we use the observed $p\text{-}NH_3(1, 1)$ linewidth as a measure of the non-thermal velocity dispersion, $\sigma_{\text{NT}} (= 169.9 \pm 4.2$ m s^{-1}), the effective sound speed becomes $c_{\text{eff}} = (c_s^2 + \sigma_{\text{NT}}^2)^{1/2} = 260.5 \pm 1.6$ m s^{-1}. The corresponding effective Jeans length is $\lambda_J^{\text{eff}} \simeq 0.06$ pc. Although not much different from the purely thermal value, λ_J^{eff} is in better agreement with the observed projected distances of SMM3b and 3c from the protostar position (0.07–0.10 pc). Hence, the parent core might have fragmented as a result of Jeans-type instability with density perturbations in a self-gravitating fluid having both the thermal and non-thermal motions (we note that in Paper III we suggested a pure thermal Jeans fragmentation scenario due to the aforementioned longer λ_J

value). Because information in the core is transported at the sound speed (being it thermal or effective one), the fragmentation timescale is expected to be comparable to the crossing time, $\tau_{cross} = R/c_{eff}$, where $R = 0.07$–0.10 pc. This is equal to $\tau_{cross} \sim 2.6$–3.8×10^5 yr, which is up to an order of magnitude longer than the estimated nominal CO depletion timescale (Sect. 4.2.3).

The present SED analysis and the previous studies (see Sect. 1) suggest that SMM3 is in the Class 0 phase of stellar evolution. Observational estimates of the Class 0 lifetime are about $\sim 1 \times 10^5$ yr (Enoch et al. 2009; Evans et al. 2009; Maury et al. 2011). In agreement with observations, Offner and Arce (2014) performed radiation-hydrodynamic simulations of protostellar evolution including outflows, and obtained Stage 0 lifetimes of 1.4–2.3×10^5 yr, where the Stage 0 represents a theoretical counterpart of the observational Class 0 classification. These observational and theoretical lifetime estimates are comparable to the fragmentation timescale of SMM3, which supports a scenario of the age of SMM3 being a few times 10^5 yr.

In the present paper, we have presented the first signatures of an outflow activity in SMM3. These are *i)* the broad lines of p-H_2CO and CH_3OH; *ii)* the warm gas (64 ± 15 K) associated with the broad-line component; and *iii)* the protrusion-like feature seen at 4.5 μm (Fig. 1, bottom right panel), which is likely related to the shock emission near the accreting protostar. Outflow activity reasserts the Class 0 evolutionary stage of SMM3 (e.g. Bontemps et al. 1996).

The 350 μm flux densities of the subcondensations SMM3b and 3c are 250 ± 60 mJy and 240 ± 60 mJy, respectively (Paper III). Assuming that the dust temperature is that resulting from the SED of SMM 3 (15.1 ± 0.1 K), and adopting the same dust model as in Sect. 4.1, in which case the dust opacity per unit dust mass at 350 μm is $\kappa_{350\,\mu m} = 7.84$ cm^2 g^{-1}, the condensation masses are only $\sim 0.06 \pm 0.01$ M$_\odot$. If we instead use as T_{dust} the gas temperature derived from ammonia, the mass estimates will become about 0.16 ± 0.05 M$_\odot$, i.e. a factor of 2.7 ± 0.9 higher. As discussed in the case of the prestellar core Orion B9–SMM6 by Miettinen and Offner (2013b), these types of very low-mass condensations are likely not able to collapse to form stars without any additional mass accretion. Instead, they could represent the precursors of substellar-mass objects or brown dwarfs (e.g. Lee et al. 2013). Alternatively, if the condensations are gravitationally unbound structures, they could disperse away in the course of time, an issue that could be solved by high-resolution molecular line observations. Finally, mechanical feedback from the protostellar outflow could affect the future evolution of the condensations (cf. the proto- and prestellar core system IRAS 05399-0121/SMM1 in Orion B9; Miettinen and Offner 2013a).

5.2 Chemical properties of SMM3

5.2.1 NH_3 and N_2H^+ abundances

The fractional abundances of the N-bearing species NH_3 and N_2H^+ we derived are $6.6 \pm 0.9 \times 10^{-8}$ and $2.9 \pm 0.9 \times 10^{-10}$. The value of $x(NH_3)$ in low-mass dense cores is typically found to be a few times 10^{-8} (e.g. Friesen et al. 2009; Busquet et al. 2009). Morgan et al. (2010) derived a mean $x(NH_3)$ value of 2.6×10^{-8} towards the protostars embedded in bright-rimmed clouds. Their sources might represent the sites of triggered star formation, and could therefore resemble the case of SMM3—a core that might have initially formed as a result of external feedback. More recently, Marka et al. (2012) found that the average NH_3 abundance in their sample of globules hosting Class 0 protostars is 3×10^{-8} with respect to H_2.[14] Compared to the aforementioned reference studies, the ammonia abundance is SMM3 appears to be elevated by a factor of about two or more, although differences in the assumptions of dust properties should be borne in mind. The chemical modelling of the Class 0 sources performed by Marka et al. (2012), which included reactions taking place on dust grain surfaces, predicted that an NH_3 abundance exceeds $\sim 10^{-8}$ after 10^5 yr of evolution (see also Hily-Blant et al. 2010 for a comparable result). This compares well with the fragmentation timescale in SMM3 estimated above. For their sample of low-mass protostellar cores, Caselli et al. (2002b) found a mean N_2H^+ abundance of $3 \pm 2 \times 10^{-10}$, which is very similar to the one we have derived for SMM3.

The $[NH_3]/[N_2H^+]$ ratio in SMM3, derived from the corresponding column densities, is 125 ± 45. The abundance ratio between these two species is known to show different values in starless and star-forming objects. For example, Hotzel et al. (2004), who studied the dense cores B217 and L1262, both associated with Class I protostars, found that the above ratio is ~ 140–190 in the starless parts of the cores, but only about ~ 60–90 towards the protostars. Our value, measured towards the outer edge of SMM3, lies in between these two ranges, and hence is consistent with the observed trend. A similar behaviour is seen in IRAS 20293+3952, a site of clustered star formation (Palau et al. 2007), and clustered low-mass star-forming core Ophiuchus B (Friesen et al. 2010). In contrast, for their sample of dense cores in Perseus, Johnstone et al. (2010) found that the p-NH_3/N_2H^+ column density ratio is fairly similar in protostellar cores (20 ± 7) and in prestellar cores (25 ± 12). Their ratios also appear to be lower than found in other sources (we note that the statistical equilibrium value of the NH_3 *ortho/para* ratio is unity; e.g. Umemoto et al. 1999).

---

[14]The authors reported the abundances with respect to the total hydrogen column density, which is here assumed to be $N_H = 2N(H_2)$.

The chemical reactions controlling the $[NH_3]/[N_2H^+]$ ratio were summarised by Fontani et al. (2012; Appendix A therein). In starless cores, the physical conditions are such that both the CO and N_2 molecules can be heavily depleted. If this is the case, N_2H^+ cannot be efficiently formed by the reaction between H_3^+ and N_2. On the other hand, this is counterbalanced by the fact that N_2H^+ cannot be destroyed by the gas-phase CO, although it would serve as a channel for the N_2 production (CO + $N_2H^+ \rightarrow HCO^+ + N_2$). Instead, in a gas with strong CO depletion, N_2H^+ is destroyed by the dissociative electron recombination. The absence of N_2 also diminishes the production of N^+, the cations from which NH_3 is ultimately formed via the reaction $NH_4^+ + e^-$. However, the other routes to N^+, namely CN + He^+ and $NH_2 + He^+$, can still operate. We also note that H_3^+, which also cannot be destroyed by CO in the case of strong CO depletion, is a potential destruction agent of NH_3. However, the end product of the reaction $NH_3 + H_3^+$ is NH_4^+, the precursor of NH_3. For these reasons, the NH_3 abundance can sustain at the level where the $[NH_3]/[N_2H^+]$ ratio is higher in starless cores (strong depletion) than in the protostellar cores (weaker depletion). It should be noted that the study of the high-mass star-forming region AFGL 5142 by Busquet et al. (2011) showed that the $[NH_3]/[N_2H^+]$ ratio behaves opposite to that in low-mass star-forming regions. The authors concluded that the higher ratio seen towards the hot core position is the result of a higher dust temperature, leading to the desorption of CO molecules from the grains mantles. As a result, the gas-phase CO can destroy the N_2H^+ molecules, which results in a higher $[NH_3]/[N_2H^+]$ ratio. Because SMM3 shows evidence for quite a strong CO depletion of $f_D = 27.3 \pm 1.8$ towards the core centre, the chemical scheme described above is probably responsible for the much higher abundance of ammonia compared to N_2H^+.

5.2.2 Depletion and deuteration

As mentioned above, the CO molecules in SMM3 appear to be quite heavily depleted towards the protostar position, while it becomes lower by a factor of 3.3 ± 0.4 towards the outer core edge. A caveat here is that the two depletion factors were derived from two different isotopologues, namely $C^{17}O$ for the envelope zone, and $C^{18}O$ towards the core centre. This brings into question the direct comparison of the two depletion factors. Indeed, although the critical densities of the detected CO isotopologue transitions are very similar, the $C^{18}O$ linewidth is 1.4 ± 0.3 times greater than that of $C^{17}O$. Although this is not a significant discrepancy, the observed $C^{18}O$ emission could originate in a more turbulent parts of the core.

For comparison, for their sample of 20 Class 0 protostellar cores, Emprechtinger et al. (2009) derived CO depletion factors of 0.3 ± 0.09–4.4 ± 1.0. These are significantly lower

than what we have derived for SMM3. The depletion factor in the outer edge of SMM3 we found is more reminiscent to those seen in low-mass starless cores (e.g. Bacmann et al. 2002; Crapsi et al. 2005), but the value towards the core's 24 μm peak position stands out as an exceptionally high.

The deuterium fractionation of N_2H^+, or the N_2D^+/N_2H^+ column density ratio, is found to be 0.14 ± 0.06 towards the core edge. This lies midway between the values found by Roberts and Millar (2007) for their sample of Class 0 protostars (0.06 ± 0.01–0.31 ± 0.05). Emprechtinger et al. (2009) found N_2D^+/N_2H^+ ratios in the range <0.029–0.271 ± 0.024 with an average value of 0.097. Among their source sample, most objects had a deuteration level of <0.1, while 20% of the sources showed values of >0.15. With respect to these results, the deuterium fractionation in SMM3 appears to be at a rather typical level among Class 0 objects. For comparison, in low-mass starless cores the N_2D^+/N_2H^+ ratio can be several tens of percent (Crapsi et al. 2005), while intermediate-mass Class 0-type protostars show values that are more than ten times lower than in SMM3 (Alonso-Albi et al. 2010). A visual inspection of Fig. 3 in Emprechtinger et al. (2009) suggests that for a N_2D^+/N_2H^+ ratio we have derived for SMM3, the dust temperature is expected to be $\lesssim 25$ K. This is qualitatively consistent with a value of 15.1 ± 0.1 K we obtained from the MBB SED fit. On the other hand, the correlation in the middle panel of Fig. 4 in Emprechtinger et al. (2009; see also their Fig. 10) suggests that the CO depletion factor would be ∼3 at the deuteration level seen in SMM3, while our observed value in the envelope is 2.8 ± 0.2 times higher. The fact that CO molecules appear to be more heavily depleted towards the new line observation target position suggests that the degree of deuterium fractionation there is also higher. A possible manifestation of this is that the estimated DCO^+ abundance is higher by a factor of 13.0 ± 7.7 towards the core centre than towards the core edge, but this discrepancy could be partly caused by the different transitions used in the analysis ($J = 3$–2 and $J = 4$–3, respectively).

Recently, Kang et al. (2015) derived a deuterium fractionation of formaldehyde in SMM3 (towards the core centre), and they found a $HDCO/H_2CO$ ratio of 0.31 ± 0.06, which is the highest value among their sample of 15 Class 0 objects. This high deuteration level led the authors to conclude that SMM3 is in a very early stage of protostellar evolution.

5.2.3 H_2CO, CH_3OH, and SO—outflow chemistry in SMM3

Besides the narrow ($\Delta v = 0.42$ km s^{-1}) component of the p-$H_2CO(3_{0,3}$–$2_{0,2})$ line detected towards SMM3, this line also exhibits a much wider ($\Delta v = 8.22$ km s^{-1}) component with blue- and redshifted wing emission. The other two transitions of p-H_2CO we detected, ($3_{2,1}$–$2_{2,0}$) and ($3_{2,2}$–$2_{2,1}$),

are also broad, more than 10 km s^{-1} in FWHM, and exhibit wing emission. The methanol line we detected, with a FWHM of 10.98 km s^{-1}, is also significantly broader than most of the lines we have detected. The similarity between the FWHMs of the methanol and formaldehyde lines suggests that they originate in a common gas component. The rotational temperature derived from the p-H$_2$CO lines, 64 ± 15 K, is considerably higher than the dust temperature in the envelope and the gas temperature derived from ammonia. The large linewidths and the relatively warm gas temperature can be understood if a protostellar outflow has swept up and shock-heated the surrounding medium.

The H$_2$CO and CH$_3$OH molecules are organic species, and they can form on dust grain surfaces through a common CO hydrogenation reaction sequence (CO → HCO → H$_2$CO → CH$_3$O or H$_3$CO or CH$_2$OH or H$_2$COH → CH$_3$OH; e.g. Watanabe and Kouchi 2002; Hiraoka et al. 2002; Fuchs et al. 2009, and references therein). The intermediate compound, solid formaldehyde, and the end product, solid methanol, have both been detected in absorption towards low-mass young stellar objects (YSOs; Pontoppidan et al. 2003; Boogert et al. 2008). A more recent study of solid-phase CH$_3$OH in low-mass YSOs by Bottinelli et al. (2010) suggests that much of the CH$_3$OH is in a CO-rich ice layer, which conforms to the aforementioned formation path. We note that H$_2$CO can also be formed in the gas phase (e.g. Kahane et al. 1984; Federman and Allen 1991), and the narrow p-H$_2$CO line we detected is likely tracing a quiescent gas not enriched by the chemical compounds formed on dust grains. The estimated p-H$_2$CO abundance for this component is very low, only $2.0 \pm 0.6 \times 10^{-11}$. We note that the total H$_2$CO column density derived by Kang et al. (2015), $N(\text{H}_2\text{CO}) = 3.3 \pm 0.4 \times 10^{12}$ cm^{-2} at $T_{\text{ex}} = 10$ K, is in good agreement with our p-H$_2$CO column density if the $ortho/para$ ratio is 3:1 as assumed by the authors.

In contrast, the fractional p-H$_2$CO abundance is found to be 155 ± 70 times higher for the broad component than for the narrow one. The origin of the H$_2$CO abundance enhancement in low-mass protostars can be understood in terms of the liberation of the ice mantles (Schöier et al. 2004). We note that there are also gas-phase formation routes for CH$_3$OH, which start from the reaction between CH$_3^+$ and H$_2$O or between H$_3$CO$^+$ and H$_2$CO. The resulting protonated methanol, CH$_3$OH$_2^+$, can recombine with an electron and dissociate to produce CH$_3$OH (Garrod et al. 2006; Geppert et al. 2006). However, the gas-phase syntheses are not able to produce the high fractional abundances like observed here towards SMM3 ($9.4 \pm 2.5 \times 10^{-8}$). The thermal desorption of CH$_3$OH requires a dust temperature of at least ~80 K (Brown and Bolina 2007; Green et al. 2009). Although highly uncertain, the H$_2$CO rotational temperature

we derived does not suggest the dust temperature to be sufficiently high for CH$_3$OH molecules to sublimate. Hence, it seems possible that an outflow driven by SMM3 has sputtered the icy grain mantles (in impacts with gas-phase H$_2$ and He) so that H$_2$CO and CH$_3$OH were released into the gas phase. On the other hand, the high CO depletion factors we derived suggest that the grain ices are rich in CO, and if CH$_3$OH molecules are embedded in CO-rich ice layers, their thermal evaporation temperature can be considerably lower (~30 K; see Maret et al. 2005).

The p-H$_2$CO/CH$_3$OH column density ratio for the broad line component is found to be 0.03 ± 0.005. This value represents a lower limit to the total H$_2$CO/CH$_3$OH ratio, which depends on the o/p ratio. Based on the observed abundances of both the $ortho$ and $para$ forms of H$_2$CO in low-mass dense cores, Jørgensen et al. (2005) derived a o/p ratio of 1.6 ± 0.3. The authors interpreted this to be consistent with thermalisation at 10–15 K on dust grains. If we assume that the o/p ratio is $\simeq 1.6$, we obtain a total H$_2$CO/CH$_3$OH column density ratio of $\simeq 0.08 \pm 0.01$, while for a o/p ratio, which is equal to the relative statistical weights of 3:1, the total H$_2$CO/CH$_3$OH ratio becomes 0.13 ± 0.02. The H$_2$CO/CH$_3$OH ice abundance ratio in low-mass YSOs is found to be in the range ~0.2–6 (Boogert et al. 2008), which is higher than the gas-phase abundance ratio towards SMM3. Hence, it is possible that the ices are not completely sublimated into the gas phase. Interestingly, if the total H$_2$CO/CH$_3$OH ratio for SMM3 is ~0.1, and $x(\text{CH}_3\text{OH}) \sim 10^{-7}$, then these properties would resemble those derived for the Galactic centre clouds where shocks (caused by expanding bubbles, cloud-cloud collisions, etc.) are believed to have ejected the species from the grain mantles (Requena-Torres et al. 2006). In contrast, for the hot interiors of Class 0 sources, i.e. hot corinos, the H$_2$CO/CH$_3$OH ratio is found to be higher, in the range >0.3–4.3 (Maret et al. 2005; their Table 3), which are comparable to the aforementioned ice abundance ratios. In hot corinos the dust temperature exceeds 100 K, and the evaporation of ice mantles is the result of radiative heating by the central protostar. Moreover, in the Horsehead photodissociation region (PDR) in Orion B, the H$_2$CO/CH$_3$OH ratio is found to be 2.3 ± 0.4 (Guzmán et al. 2013). Guzmán et al. (2013) concluded that in the UV-illuminated PDR both H$_2$CO and CH$_3$OH are released from the grain mantles through photodesorption.

The SO line we detected is narrow ($\Delta v = 0.68$ km s^{-1}), but low-intensity wing emission can be seen on both sides of it (see Codella et al. 2002 for similar spectra towards the CB34 globule, which harbours a cluster of Class 0 objects). The derived fractional abundance of SO, $1.6 \pm 0.2 \times 10^{-10}$, is very low, as for example the average abundance derived by Buckle and Fuller (2003) for their sample of Class 0 objects is $3.1 \pm 0.9 \times 10^{-9}$, and in the starless TMC-1 cloud the abundance is found to be ~10^{-8} (Lique et al. 2006).

While our narrow SO line is probably originating in the quiescent envelope, where SO is formed through the reactions $S + OH$ and $S + O_2$ (e.g. Turner 1995), the weak line wings provide a hint of an outflowing SO gas. The SO emission is indeed known to be a tracer of protostellar outflows (e.g. Chernin et al. 1994; Lee et al. 2010; Tafalla and Hacar 2013). Outflow shocks can first release H_2S molecules from dust grains, and subsequent hydrogenation reactions produce HS molecules and S atoms ($H_2S + H \rightarrow HS + H_2$; $HS + H \rightarrow S + H_2$; Mitchell 1984; Charnley 1997). The oxidation reactions $HS + O$ and $S + O_2$ can then lead to the formation of SO (see Bachiller et al. 2001). For example, Lee et al. (2010) derived an SO abundance of $\sim 2 \times 10^{-6}$ towards the HH211 jet driven by a Class 0 protostar, which shows that a significant abundance enhancement can take place in low-mass outflows. Some of the evolutionary models of the sulphur chemistry by Buckle and Fuller (2003) suggest that, after $\sim 10^5$ yr, the abundance of H_2S starts to drop, which leads to a rapid decrease in the SO abundance. This could explain the very weak SO wing emission seen towards SMM3, and agrees with the observational estimates of the Class 0 lifetime of about $\sim 1 \times 10^5$ yr (e.g. Evans et al. 2009; see also Offner and Arce 2014 for a comparable result from simulations). Interestingly, some of the Buckle and Fuller (2003) models, for example the one with a gas temperature of 10 K, H_2 density of 10^5 cm^{-3}, and a cosmic-ray ionisation rate of $\zeta_H = 1.3 \times 10^{-16}$ s^{-1}, which is ten times the standard ζ_H (their Fig. 7, bottom left), predict SO abundances comparable to that observed in SMM3 (a few times 10^{-10}) after 10^5 yr, so perhaps the narrow-line component could also be (partly) tracing a gas component that was affected by outflows in the past.

6 Summary and conclusions

We used the APEX telescope to carry out follow-up molecular line observations towards the protostellar core SMM3, which is embedded in the filamentary Orion B9 star-forming region. The new data were used in conjunction with our earlier APEX data (including SABOCA and LABOCA continuum data), and NH_3 observations from the Effelsberg 100 m telescope. The main results are summarised as follows.

1. From the observed frequency range ~ 218.2–222.2 GHz, the following chemical compounds were identified: ^{13}CO, $C^{18}O$, SO, p-H_2CO, and CH_3OH-E_1. The last two species play a key role in the synthesis of more complex organic molecules and prebiotic chemistry, which makes them particularly interesting compounds in the gas reservoir of a solar-type protostar like SMM3. Our new mapping observations of SMM3 were performed in the frequency range ~ 215.1–219.1 GHz, from which

DCO$^+$(3–2) and p-$H_2CO(3_{0,3}$–$2_{0,2})$ lines were identified.

2. Our revised SED analysis of SMM3 supports its Class 0 classification. The dust temperature, envelope mass, and luminosity were derived to be 15.1 ± 0.1 K, 3.1 ± 0.6 M$_\odot$, and 3.8 ± 0.6 L$_\odot$. The NH_3-based gas kinetic temperature was derived to be $T_{kin} = 11.2 \pm 0.5$ K. The revised analysis of the subfragments seen in our SABOCA 350 μm map suggests that SMM3 went through a Jeans-type fragmentation phase, where the initial density perturbations might have had contributions from both thermal and non-thermal motions.

3. The CO depletion factor derived from the new $C^{18}O$ data towards the core centre is very high, 27.3 ± 1.8, while that re-computed from our previous $C^{17}O$ data towards the core edge is clearly lower, 8.3 ± 0.7. We also recalculated the degree of deuterium fractionation in the latter position, in terms of the N_2D^+/N_2H^+ ratio, and found a value of 0.14 ± 0.06. Even higher deuteration is to be expected towards the new line observation target position because of the stronger CO freeze out.

4. The new spectral-line mapping observations revealed that SMM3 is associated with extended DCO$^+$ and p-H_2CO emission (as compared with the 350 μm-emitting region), and both the line emissions appear to be elongated in the east-west direction. Besides the systemic velocity of ~ 8.5 km s^{-1}, emission from p-$H_2CO(3_{0,3}$–$2_{0,2})$ was also detected at a radial velocity of 1.5 km s^{-1}, which concentrates to the east and northeast of SMM3, similarly to the spatial distributions of $^{13}CO(2$–$1)$ and $C^{18}O(2$–$1)$ seen earlier by Miettinen (2012b).

5. The single-pointing observations showed that the $3_{0,3}$–$2_{0,2}$ line of p-H_2CO exhibits two components, a narrow one and a broad one. The other two p-H_2CO lines we detected, $3_{2,1}$–$2_{2,0}$ and $3_{2,2}$–$2_{2,1}$, are also broad. Hence, a rotational diagram was constructed for the broad component of p-H_2CO, which yielded a rotational temperature of 64 ± 15 K. The detected methanol line has a width comparable to those of the broad formaldehyde lines, and is hence likely tracing the same warm gas component.

6. We interpret the broad p-H_2CO and CH_3OH lines, and the elevated gas temperature, to be the first clear evidence of shock processing and outflow activity in SMM3. The abundance of p-H_2CO in the broad component is enhanced by two orders of magnitude with respect to the quiescent gas component. Additionally, the protrusion-like emission feature seen in the *Spitzer* 4.5 μm image is likely related to shock emission.

7. The detected SO line shows a narrow component at the systemic velocity, and weak wings on both sides of it. The wing emission points towards a weak SO outflow, while the narrow component is probably tracing the quiescent envelope.

8. The estimated fragmentation timescale of SMM3, and the observed chemical characteristics all suggest that the age of SMM3 is a few times 10^5 yr, in agreement with its inferred Class 0 evolutionary stage. A dedicated chemical modelling would be useful in setting tighter constraints on the source age.

Putting the results from the previous studies and the present one together, we are in a position to place SMM3 in the wider context of Class 0 objects. Stutz et al. (2013) classified SMM3 as a so-called PACS Bright Red source, or PBRs. This source population is composed of extreme, red Class 0 objects with presumably high-density envelopes and high mass infall rates, and the median values of their MBB-based dust temperature, envelope mass, luminosity, and L_{submm}/L ratio are 19.6 K, 0.6 $M_\odot$, 1.8 $L_\odot$, and 2.7% (see Table 8 in S13).[15] Although the physical properties of SMM3 we have derived in the present work are more extreme than the typical PBRs' properties (it is colder, more massive, and more luminous), it can still be classified as a PBRs in agreement with S13 because this population was also found to contain sources with properties comparable to those we have derived. We note that the Orion B cloud appears to contain a relatively high fraction of PBRs-type objects (17% of the known protostars in Orion B) compared to that in Orion A (1%; S13).

We can also draw a conclusion that SMM3 exhibits a rich chemistry. It is possible that this Class 0 protostellar core hosts a so-called hot corino where the gas-phase chemistry can be as rich as in the hot molecular cores associated with high-mass star formation. This can be tested through high resolution interferometric multi-line observations. Such observations would also be useful to examine whether SMM3 drives a chemically rich/active molecular outflow, as our detection of the broad formaldehyde and methanol lines already suggest. In a more general context of low-mass star formation, SMM3 has the potential to become a useful target source of chemical evolution in a triggered star-forming region (feedback from NGC 2024, which could be ultimately linked to the nearby Ori OB1 association within the Ori-Eri superbubble). By comparing its properties with those of Class 0 objects in more isolated, quiescent regions, it could be possible to investigate whether its (chemical) evolution could have been accelerated as a result of more dynamic environment. The observed fragmentation of the SMM3 core indeed suggests that it has had a dynamical history, and is a fairly atypical object compared to the general Class 0 population in the Galaxy.

---

[15]We note that these median values were calculated by including the SMM3 values derived by S13, but if they are omitted, the median values are essentially the same. The median envelope mass reported here was scaled to the presently assumed dust-to-gas ratio.

References

Alonso-Albi, T., Fuente, A., Crimier, N., et al.: Astron. Astrophys. **518**, A52 (2010)

Alves, J., Lombardi, M., Lada, C.J.: Astron. Astrophys. **462**, L17 (2007)

Anderson, I.M., Caselli, P., Haikala, L.K., Harju, J.: Astron. Astrophys. **347**, 983 (1999)

André, P., Ward-Thompson, D., Barsony, M.: Astrophys. J. **406**, 122 (1993)

André, P., Ward-Thompson, D., Barsony, M.: In: Mannings, V., Boss, A.P., Russell, S.S. (eds.) Protostars and Planets IV, p. 59. University of Arizona Press, Tucson (2000)

André, P., Men'shchikov, A., Bontemps, S., et al.: Astron. Astrophys. **518**, L102 (2010)

Bachiller, R., Pérez Gutiérrez, M., Kumar, M.S.N., Tafalla, M.: Astron. Astrophys. **372**, 899 (2001)

Bacmann, A., Lefloch, B., Ceccarelli, C., et al.: Astron. Astrophys. **389**, L6 (2002)

Belitsky, V., Lapkin, I., Vassilev, V., et al.: In: Proc. of Joint 32nd International Conference on Infrared Millimeter Waves and 15th International Conference on Terahertz Electronics, September 3–7, 2007, City Hall, Cardiff, Wales, UK, p. 326 (2007)

Bertsimas, D., Tsitsiklis, J.N.: Stat. Sci. **8**(1), 10–15 (1993)

Bontemps, S., André, P., Terebey, S., Cabrit, S.: Astron. Astrophys. **311**, 858 (1996)

Boogert, A.C.A., Pontoppidan, K.M., Knez, C., et al.: Astrophys. J. **678**, 985 (2008)

Bottinelli, S., Boogert, A.C.A., Bouwman, J., et al.: Astrophys. J. **718**, 1100 (2010)

Brown, W.A., Bolina, A.S.: Mon. Not. R. Astron. Soc. **374**, 1006 (2007)

Buckle, J.V., Fuller, G.A.: Astron. Astrophys. **399**, 567 (2003)

Busquet, G., Palau, A., Estalella, R., et al.: Astron. Astrophys. **506**, 1183 (2009)

Busquet, G., Estalella, R., Zhang, Q., et al.: Astron. Astrophys. **525**, A141 (2011)

Caselli, P., Walmsley, C.M., Zucconi, A., et al.: Astrophys. J. **565**, 331 (2002a)

Caselli, P., Benson, P.J., Myers, P.C., Tafalla, M.: Astrophys. J. **572**, 238 (2002b)

Cazzoli, G., Puzzarini, C., Lapinov, A.V.: Astrophys. J. **611**, 615 (2004)

Charnley, S.B.: Astrophys. J. **481**, 396 (1997)

Chernin, L.M., Masson, C.R., Fuller, G.A.: Astrophys. J. **436**, 741 (1994)

Codella, C., Scappini, F., Bachiller, R., Benedettini, M.: Mon. Not. R. Astron. Soc. **331**, 893 (2002)

Coutens, A., Persson, M.V., Jørgensen, J.K., et al.: Astron. Astrophys. **576**, A5 (2015)

Cowie, L.L., Songaila, A., York, D.G.: Astrophys. J. **230**, 469 (1979)

Crapsi, A., Caselli, P., Walmsley, C.M., et al.: Astrophys. J. **619**, 379 (2005)

Daniel, F., Gérin, M., Roueff, E., et al.: Astron. Astrophys. **560**, A3 (2013)

De Buizer, J.M., Vacca, W.D.: Astron. J. **140**, 196 (2010)

Emprechtinger, M., Caselli, P., Volgenau, N.H., Stutzki, J., Wiedner, M.C.: Astron. Astrophys. **493**, 89 (2009)

Enoch, M.L., Evans, N.J. II, Sargent, A.I., Glenn, J.: Astrophys. J. **692**, 973 (2009)

Evans, N.J. II, Dunham, M.M., Jørgensen, J.K., et al.: Astrophys. J. Suppl. Ser. **181**, 321 (2009)

Fazio, G.G., Hora, J.L., Allen, L.E., et al.: Astrophys. J. Suppl. Ser. **154**, 10 (2004)

Federman, S.R., Allen, M.: Astrophys. J. **375**, 157 (1991)

Fixsen, D.J.: Astrophys. J. **707**, 916 (2009)

Fontani, F., Caselli, P., Zhang, Q., et al.: Astron. Astrophys. **541**, A32 (2012)

Friesen, R.K., Di Francesco, J., Shirley, Y.L., Myers, P.C.: Astrophys. J. **697**, 1457 (2009)

Friesen, R.K., Di Francesco, J., Shimajiri, Y., Takakuwa, S.: Astrophys. J. **708**, 1002 (2010)

Fuchs, G.W., Cuppen, H.M., Ioppolo, S., et al.: Astron. Astrophys. **505**, 629 (2009)

Furlan, E., Fischer, W.J., Ali, B., et al.: Astrophys. J. Suppl. Ser. **224**, 5 (2016)

Garrod, R., Park, I.H., Caselli, P., Herbst, E.: Faraday Discussions, vol. 133, p. 51 (2006)

Geppert, W.D., Hamberg, M., Thomas, R.D., et al.: Faraday Discussions, vol. 133, p. 177 (2006)

Goldsmith, P.F., Langer, W.D.: Astrophys. J. **517**, 209 (1999)

Green, S.D., Bolina, A.S., Chen, R., et al.: Mon. Not. R. Astron. Soc. **398**, 357 (2009)

Green, J.D., Evans, N.J. II, Jørgensen, J.K., et al.: Astrophys. J. **770**, 123 (2013)

Guzmán, V.V., Goicoechea, J.R., Pety, J., et al.: Astron. Astrophys. **560**, A73 (2013)

Güsten, R., Nyman, L.Å., Schilke, P., et al.: Astron. Astrophys. **454**, L13 (2006)

Hacar, A., Tafalla, M.: Astron. Astrophys. **533**, A34 (2011)

Harju, J., Walmsley, C.M., Wouterloot, J.G.A.: Astron. Astrophys. Suppl. Ser. **98**, 51 (1993)

Hily-Blant, P., Maret, S., Bacmann, A., et al.: Astron. Astrophys. **521**, L52 (2010)

Hiraoka, K., Sato, T., Sato, S., et al.: Astrophys. J. **577**, 265 (2002)

Ho, P.T.P., Barrett, A.H., Myers, P.C., et al.: Astrophys. J. **234**, 912 (1979)

Hollenbach, D., McKee, C.F.: Astrophys. J. **342**, 306 (1989)

Hotzel, S., Harju, J., Walmsley, C.M.: Astron. Astrophys. **415**, 1065 (2004)

Ireland, J.: Sol. Phys. **243**, 237 (2007)

Johnstone, D., Rosolowsky, E., Tafalla, M., Kirk, H.: Astrophys. J. **711**, 655 (2010)

Jørgensen, J.K., Schöier, F.L., van Dishoeck, E.F.: Astron. Astrophys. **437**, 501 (2005)

Jørgensen, J.K., Favre, C., Bisschop, S.E., et al.: Astrophys. J. Lett. **757**, L4 (2012)

Kahane, C., Lucas, R., Frerking, M.A., et al.: Astron. Astrophys. **137**, 211 (1984)

Kang, M., Choi, M., Stutz, A.M., Tatematsu, K.: Astrophys. J. **814**, 31 (2015)

Kirkpatrick, S., Gelatt, C.D., Vecchi, M.P.: Science **220**, 671 (1983)

Klein, B., Hochgürtel, S., Krämer, I., et al.: Astron. Astrophys. **542**, L3 (2012)

Kontinen, S., Harju, J., Heikkilä, A., Haikala, L.K.: Astron. Astrophys. **361**, 704 (2000)

Kovács, A.: Proc. SPIE **7020**, 45 (2008)

Lacy, J.H., Knacke, R., Geballe, T.R., Tokunaga, A.T.: Astrophys. J. Lett. **428**, L69 (1994)

Ladd, E.F., Fuller, G.A., Deane, J.R.: Astrophys. J. **495**, 871 (1998)

Lai, S.-P., Velusamy, T., Langer, W.D., Kuiper, T.B.H.: Astron. J. **126**, 311 (2003)

Lee, C.-F., Hasegawa, T.I., Hirano, N., et al.: Astrophys. J. **713**, 731 (2010)

Lee, C.W., Kim, M.-R., Kim, G., et al.: Astrophys. J. **777**, 50 (2013)

Linke, R.A., Frerking, M.A., Thaddeus, P.: Astrophys. J. Lett. **234**, L139 (1979)

Lique, F., Cernicharo, J., Cox, P.: Astrophys. J. **653**, 1342 (2006)

Mangum, J.G., Wootten, A., Mundy, L.G.: Astrophys. J. **388**, 467 (1992)

Maret, S., Ceccarelli, C., Tielens, A.G.G.M., et al.: Astron. Astrophys. **442**, 527 (2005)

Maret, S., Faure, A., Scifoni, E., Wiesenfeld, L.: Mon. Not. R. Astron. Soc. **399**, 425 (2009)

Maret, S., Hily-Blant, P., Pety, J., et al.: Astron. Astrophys. **526**, A47 (2011)

Marka, C., Schreyer, K., Launhardt, R., et al.: Astron. Astrophys. **537**, A4 (2012)

Maury, A.J., André, P., Men'shchikov, A., et al.: Astron. Astrophys. **535**, A77 (2011)

McKee, C.F., Ostriker, E.C.: Annu. Rev. Astron. Astrophys. **45**, 565 (2007)

Miettinen, O.: Astron. Astrophys. **542**, A101 (2012a)

Miettinen, O.: Astron. Astrophys. **545**, A3 (2012b)

Miettinen, O., Offner, S.S.R.: Astron. Astrophys. **553**, A88 (2013a)

Miettinen, O., Offner, S.S.R.: Astron. Astrophys. **555**, A41 (2013b)

Miettinen, O., Harju, J., Haikala, L.K., et al.: Astron. Astrophys. **500**, 845 (2009). Paper I

Miettinen, O., Harju, J., Haikala, L.K., Juvela, M.: Astron. Astrophys. **524**, A91 (2010). Paper II

Miettinen, O., Harju, J., Haikala, L.K., Juvela, M.: Astron. Astrophys. **538**, A137 (2012). Paper III

Milam, S.N., Savage, C., Brewster, M.A., et al.: Astrophys. J. **634**, 1126 (2005)

Mitchell, G.F.: Astrophys. J. **287**, 665 (1984)

Morgan, L.K., Figura, C.C., Urquhart, J.S., Thompson, M.A.: Mon. Not. R. Astron. Soc. **408**, 157 (2010)

Müller, H.S.P., Schlöder, F., Stutzki, J., Winnewisser, G.: J. Mol. Struct. **742**, 215 (2005)

Myers, P.C., Ladd, E.F.: Astrophys. J. Lett. **413**, L47 (1993)

Offner, S.S.R., Arce, H.G.: Astrophys. J. **784**, 61 (2014)

Ossenkopf, V., Henning, T.: Astron. Astrophys. **291**, 943 (1994)

Pagani, L., Daniel, F., Dubernet, M.-L.: Astron. Astrophys. **494**, 719 (2009)

Palau, A., Estalella, R., Girart, J.M., et al.: Astron. Astrophys. **465**, 219 (2007)

Pickett, H.M., Poynter, R.L., Cohen, E.A., et al.: J. Quant. Spectrosc. Radiat. Transf. **60**, 883 (1998)

Pilbratt, G.L., Riedinger, J.R., Passvogel, T., et al.: Astron. Astrophys. **518**, L1 (2010)

Poglitsch, A., Waelkens, C., Geis, N., et al.: Astron. Astrophys. **518**, L2 (2010)

Pontoppidan, K.M., Dartois, E., van Dishoeck, E.F., et al.: Astron. Astrophys. **404**, L17 (2003)

Ragan, S., Henning, T., Krause, O., et al.: Astron. Astrophys. **547**, A49 (2012)

Requena-Torres, M.A., Martín-Pintado, J., Rodríguez-Franco, A., et al.: Astron. Astrophys. **455**, 971 (2006)

Rieke, G.H., Young, E.T., Engelbracht, C.W., et al.: Astrophys. J. Suppl. Ser. **154**, 25 (2004)

Ripple, F., Heyer, M.H., Gutermuth, R., et al.: Mon. Not. R. Astron. Soc. **431**, 1296 (2013)

Roberts, H., Millar, T.J.: Astron. Astrophys. **471**, 849 (2007)

Savage, C., Apponi, A.J., Ziurys, L.M., Wyckoff, S.: Astrophys. J. **578**, 211 (2002)

Schneider, N., André, P., Könyves, V., et al.: Astrophys. J. Lett. **766**, L17 (2013)

Schöier, F.L., Jørgensen, J.K., van Dishoeck, E.F., Blake, G.A.: Astron. Astrophys. **418**, 185 (2004)

Schöier, F.L., van der Tak, F.F.S., van Dishoeck, E.F., Black, J.H.: Astron. Astrophys. **432**, 369 (2005)

Shu, F.H., Adams, F.C., Lizano, S.: Annu. Rev. Astron. Astrophys. **25**, 23 (1987)

Smith, M.D., Rosen, A.: Mon. Not. R. Astron. Soc. **357**, 1370 (2005)

Stahler, S.W., Palla, F.: The Formation of Stars. Wiley-VCH, Weinheim (2005)

Stutz, A.M., Tobin, J.J., Stanke, T., et al.: Astrophys. J. **767**, 36 (2013). S13

Tafalla, M., Myers, P.C., Caselli, P., Walmsley, C.M.: Astron. Astrophys. **416**, 191 (2004)

Tafalla, M., Hacar, A.: Astron. Astrophys. **552**, L9 (2013)

Tiemann, E.: J. Phys. Chem. Ref. Data **3**, 259 (1974)

Tobin, J.J., Stutz, A.M., Megeath, S.T., et al.: Astrophys. J. **798**, 128 (2015)

Townes, C.H., Schawlow, A.L.: Microwave Spectroscopy. Dover Publications, New York (1975)

Turner, B.E.: Astrophys. J. Suppl. Ser. **76**, 617 (1991)

Turner, B.E.: Astrophys. J. **455**, 556 (1995)

Umemoto, T., Mikami, H., Yamamoto, S., Hirano, N.: Astrophys. J. Lett. **525**, L105 (1999)

van der Tak, F.F.S., Müller, H.S.P., Harding, M.E., Gauss, J.: Astron. Astrophys. **507**, 347 (2009)

Vassilev, V., Meledin, D., Lapkin, I., et al.: Astron. Astrophys. **490**, 1157 (2008a)

Vassilev, V., Henke, D., Lapkin, I., et al.: IEEE Microw. Wirel. Compon. Lett. **18**, 55 (2008b)

Ward-Thompson, D., Kirk, J.M., Greaves, J.S., André, P.: Mon. Not. R. Astron. Soc. **415**, 2812 (2011)

Watanabe, N., Kouchi, A.: Astrophys. J. Lett. **571**, L173 (2002)

Wilson, T.L.: RPPh **62**, 143 (1999)

Wouterloot, J.G.A., Henkel, C., Brand, J., Davis, G.R.: Astron. Astrophys. **487**, 237 (2008)

Ybarra, J.E., Lada, E.A.: Astrophys. J. Lett. **695**, L120 (2009)

Yıldız, U.A., Kristensen, L.E., van Dishoeck, E.F., et al.: Astron. Astrophys. **556**, A89 (2013)